Received: 8 July 2023 | Revised: 10 November 2023 | Accepted: 16 December 2023

IET Smart Grid

DOI: 10.1049/stg2.12153

The Institution of Engineering and Technology WILEY

ORIGINAL RESEARCH

Machine learning autoencoder-based parameters prediction for solar power generation systems in smart grid

Ahsan Zafar[1] | Yanbo Che[1] | Muhammad Faheem[2] | Muhammad Abubakar[1] | Shujaat Ali[1] | Muhammad Shoaib Bhutta[3]

[1]Key Laboratory of Smart Grid of Ministry of Education, School of Electrical and Information Engineering, Tianjin University, Tianjin, China

[2]Department of Computing Sciences, School of Technology and Innovations, University of Vaasa, Vaasa, Finland

[3]School of Automobile Engineering, Guilin University of Aerospace Technology, Guilin, China

Correspondence

Muhammad Faheem, Department of Computing Sciences, School of Technology and Innovations, University of Vaasa, Vaasa 65200, Finland.
Email: muhammad.faheem@uwasa.fi

Abstract

During the fourth energy revolution, artificial intelligence implementation is necessary in all fields of technology to meet the increasing energy demands and address the diminishing fossil fuel reserves, necessitating the shift towards smart grids. The authors focus on predicting parameters accurately to minimise loss and improve power generation capacity in smart grids, given that accurate parameter prediction is essential for traditional power grid stations converting to smart grids. The authors employ an artificial intelligence-based machine learning model, namely the long short-term memory, to predict parameters of a solar power plant. After analysing the results obtained from the long short-term memory model in graphical visualisation, the model is further improved using two different techniques namely, a convolutional neural network-long short-term memory and the authors proposed an autoencoder long short-term memory. Comparing the results of these models, the study finds that autoencoder long short-term memory outperforms the convolutional neural network-long short-term memory as well as simple long short-term memory. Thus, the use of artificial intelligence in this study substantially enhances the precision of parameter prediction by augmenting the performance of rudimentary machine learning models, thereby facilitating the attainment of a resilient and resourceful power system that overcomes power losses and ameliorates production capacity in the context of Smart Grids.

KEYWORDS

power grids, power system management, power system planning, solar power stations

1 | INTRODUCTION

Renewable energy is rapidly gaining importance as the fossil fuel resources are depleting. The inclusion of green energy sources into smart networks has become essential to ensuring a consistent and effective supply of electricity. However, to achieve the full potential of these resources, it is essential to control smart grids through advanced technologies like artificial intelligence (AI) [1]. Among different renewable energy sources, solar plants are significant suppliers to meet energy demands. Every day, these plants produce electricity, which is supplied to the nationwide grids [2]. However, it is difficult to anticipate the generation of energy accurately in solar facilities [3]. While numerous established techniques are used to forecast power generation and other factors, the need for improvement in accuracy persists [4]. Recent years have seen researchers utilised different machine learning (ML) obtained from various electricity or energy plants [5]. These models have been demonstrated to be quite successful at predicting and forecasting many factors [6, 7]. The LSTM model demonstrated the lowest error rate compared to various other time-series forecasting models (Linear Regression, Autoregressive Integrated Moving Average [ARIMA], Seasonal Autoregressive Integrated Moving Average [SARIMA], Autoregressive Integrated Moving Average with Exogenous Variables [ARIMAX], Seasonal Autoregressive Integrated Moving Average with Exogenous

Variables [SARIMAX]) when predicting photovoltaic (PV) power generation output [8] but required fine-tuning and ensemble models to enhance efficiency. Implementation of improved ML models are not only used in the field of smart grids but also utilised in energy storage applications such as for the frequency modulation approach to optimum coordination is captured, to develop the index of voltage stability and comparable single-port models and many other industrial applications [9–12]. As in the medical field, a new deep-learning method for recovering excellent cardiac multiple regression (MR) pictures from k-space data that were severely under-sampled [13]. The approach uses a convolutional recurrent neural network (RNN) architecture that efficiently models the recurrence of the iterative reconstruction stages and learns spatio-temporal dependencies. While the approach outperforms other state-of-the-art methods, it is limited to cardiac MR images and lacks interpretability analysis. The convolutional neural network long short-term memory (CNN LSTM) hybrid model outperforms artificial neural network (ANN) and RNN models when predicting solar energy variables (SEVs), such as power generation, soiling loss, and performance ratio, demonstrating its capability as a more accurate forecasting model for power generation and performance ratio values [14], While expanding the dataset and incorporating diverse data, there is limitations in the availability and quality of such data. Similarly, the proposed CNN-LSTM model surpasses standard ML and single deep learning models in terms of prediction accuracy, precision, and stability as evaluated by error metrics, such as mean absolute error (MAE), Mean Absolute Percentage Error, and root mean square error (RMSE) [15]. In ref. [16], the hybrid framework, combining a CNN for local correlations, an Attention-based Long Short-Term Memory network for non-linear time-series characteristics of weather conditions and energy sources, and an autoregression model for linear time-series characteristics, outperforms other advanced models like ANNs and decision trees in accurately forecasting power generation from multiple renewable energy sources with neglecting the regional dependency patterns between different renewable systems. Also, in the field of weather forecasting, a deep learning encoder–decoder architectures are used in ref. [17]. The study, proposes a structure for ML, Hurri cast, for enhancing prediction of tropical cyclone track and intensity by using multiple ML encoder–decoder methods and multiple data sources. The approach achieves comparable accuracy and expertise to use the most recent operational forecast models while quickly computing and has the potential to improve the official forecast from the National Hurricane Centre. However, the study is limited in its evaluation of only route and strength forecasts with a 24-h anticipation period in specific regions. In the same way ref. [18] offers a comprehensible dam movement prediction model based on a structure consisting of encoders and decoders for mixed attention mechanism long short-term memory (MAM-LSTM). The model uses factor and temporal attention mechanisms to adaptively select influential factors and extract key time segments, while providing physical interpretation through the measurement and display of interest weights [19]. The only limitations hindering the practical application of ML ways to check the health of dam include static modelling methods, failure to adjust to the dam displacement's unpredictable character, lack of adaptive differentiation of segments and influencing factors, and black-box models' absence of actual comprehension which are needed to be improved further by improving the ML models. Similarly, a hybrid ML encoder–decoder architecture is used for dynamic energy prediction at a thermal energy facility in ref. [20]. In the study, different deep learning models anticipate the heat collected by steam and water in a boiler across multiple steps, with a focus on a new hybrid ML model by using an encoder–decoder and based on physics architecture that performs the most accurately overall. The basic flaw in the study is that initial input path must be used as the foundation for the sensitivity analysis, and further work is needed to expand the available data set and types of models investigated. A comparison of simple ML models, such as gradient-boosted regression trees (GBRT) and feed forward neural networks (FFNN) is shown in ref. [21] with LSTM autoencoder model. Resultantly LSTM autoencoder models were found to be superior to state-of-the-art techniques but RMSE is slightly higher. The study [22, 23] utilised computer vision algorithms including Fused Additive Seasonal Trend, Scale-Invariant Feature Transform, SURF, Brute Force, Fast Library for Approximate Nearest Neighbors, and autoencoder along with support vector machines (SVMs) to accurately estimate wind turbine angular velocity, and to extract a data structure that is acceptable and enables for compression by incorporating non-linear compression techniques that may improve the compression ratio while maintaining a comparable level of reconstructive accuracy respectively with the autoencoder outperforming other feature extraction methods. Also, in ref. [24], a similar study has used the autoencoder technique in which the proposed deep learning model, utilising LSTM networks and autoencoder, accurately forecasts the day-ahead solar plant output by estimating uncertainties and managing data noise. The hybrid model combining persistence and autoencoder LSTM outperforms existing methods, with the autoencoder LSTM self-supervised learning structure proving effective in predicting complex weather conditions. In a very similar way, the ML models in refs. [25–28] is utilised to forecast photovoltaic, or PV system power output. Among the three ML models employed for solar power production forecasting, the hybrid Autoencoder-Long Short-Term Memory (AE-LSTM) model demonstrated higher accuracy, outperforming the LSTM and Bi-LSTM models. This advantage is attributed to the hybrid model's capacity to identify complex temporal patterns and relationships in the data, as well as its further training, which solidified its superiority over other models [29]. Similarly, the hybrid method combining an LSTM neural network and an autoencoder for solar energy forecasting outperformed state-of-the-art models, demonstrating its superior predictive capabilities by effectively capturing both temporal and spatial features in the data [30]. Also, in ref. [31], the study introduces an LSTM autoencoder (AE) model for PV power forecasting, and the experimental results using a 23.40 kW PV power plants

dataset from Australia have demonstrated that the LSTM-AE model outperforms benchmark deep learning methods in terms of various performance measures, including MAE, RMSE, and R-squared. These models use different sets of input features, such as panel of surface, temperature, accumulation of energy, solar radiation, temperature, humidity, irradiance, cloudiness index, and past solar energy to effectively forecast Solar energy generation.

Predicting solar energy generation accurately enhances smart grid integration. However, predicting the generation of solar energy is a difficult task because of the unstable nature of this energy and its non-stability in production. In this study, we presented our suggested approach, which combines an autoencoder with an LSTM neural network, to address this difficulty. This study focuses on the usage of solar plant data collected in real-time over a period of 1 year to forecast three crucial parameters: 'daily power generation', 'grid connected power generation', and 'radiance'. These parameters can be predicted and it is achieved through the application of ML LSTM model which are further enhanced by the use of two different techniques a CNN LSTM and autoencoder LSTM. To provide an effective comparison, the outcomes of the models are contrasted. These are this study's key contributions:

- The key finding indicates that our proposed autoencoder LSTM model outperforms the two other reference models, namely LSTM and CNN LSTM, when it comes to forecasting power generation in solar across several parameters. The autoencoder LSTM model is an innovative architecture that combines the memory retention properties of LSTM networks with the feature extraction powers of autoencoders.
- The research utilises performance indicators, including MAE, mean square error (MSE), and RMSE, to assess the models' efficacy. The findings consistently reveal that the autoencoder LSTM model surpasses both the LSTM and CNN LSTM models when evaluated across various parameters, such as 'daily power generation', 'grid connected power generation' and 'radiance'.
- Enhancing the precision of forecasts through the autoencoder LSTM model is a vital contribution in solar power generation. This improvement plays a critical role in bolstering economic processes for making decisions concerning solar plant and resource allocation optimisation.
- The autoencoder LSTM model holds promise for enhancing the incorporation of renewable energy into smart grids. The use of AI significantly improves parameter prediction precision and contributes to the development of a resilient and efficient power system within the context of Smart Grids, aligning with sustainability goals.

The forthcoming Section 2 expounds the proposed methodology in detail and highlights the structure, advantages and drawbacks of the models used for prediction. The case study is presented in Section 3, where data collection process and the nature of the data using graphical visualisations is discussed. The results and errors are presented in Section 4, while Section 5 concludes the entire study.

2 | METHODOLOGY

An LSTM, CNN LSTM and autoencoder LSTM ML model were used to examine a static time series dataset in this work. For this study, we used daily power output data from a large-scale facility of solar power collected during the span of 1 year as our dataset. Preprocessing was performed to make sure the dataset fit the criteria for a stationary time series. Part of the dataset was used to teach all the models, whereas sample and validation datasets were created for the remaining data. After that, the models were assessed based on their test set results, with any necessary tweaks made to improve precision. The models' ability to correctly predict values in the validation set was tested. Then these models were used to make predictions about power production for the next year once they had been refined and validated. Forecasts of the dependent variable's future values were made using the models' predictions, which were in turn extrapolated from the time series data. The primary focus of the LSTM model was to make accurate predictions about future power generation. These predictions can be valuable for solar power plant operators as they help in resource allocation and pricing decisions. Additionally, the integration of AI into smart grids offers several benefits, including improved energy management, accurate power output predictions, enhanced grid stability, and reliable integration of renewable energy sources. AI empowers utilities to make intelligent decisions, leading to a more efficient and sustainable energy infrastructure. It was found in this research that adding an autoencoder to the LSTM model improved accuracy and decreased both MAE and MSE as compared to CNN LSTM and LSTM.

Obtaining the forecasted visual outcomes from the models is depicted in detail in the flowchart shown in Figure 1.

This study presents a technical methodology aimed at developing a predictive technique for forecasting power generation and plant performance and also involves the collection of 1 year's worth of data from a solar farm in real time, encompassing three crucial metrics: 'daily power generation', 'grid connected power', and 'radiance'. Each of these crucial parameters contains approximately 365 values, representing a 12-month data set. To accomplish the predictive task, we develop three AI techniques using Python: the LSTM, the CNN LSTM and the autoencoder LSTM. Initially, the imported data undergoes an initial analysis to assess its quality and condition. In this validation process, we verify that the data is in numerical format, as time series analysis requires numerical data without any inconsistencies (e.g. no negative numbers). Next, we partition 80% (10 months) of the data for training the deep learning LSTM, CNN LSTM and our proposed autoencoder LSTM models separately. The suitability of this training data is evaluated to ensure its compatibility with the created models. The remaining 20% (2 months) of the data is used for generating final predictions and visualisations. These visualisations combine graphical representations of the predicted results.

Comparative analysis reveals that the AI deep learning model of autoencoder LSTM exhibits lower percentages of

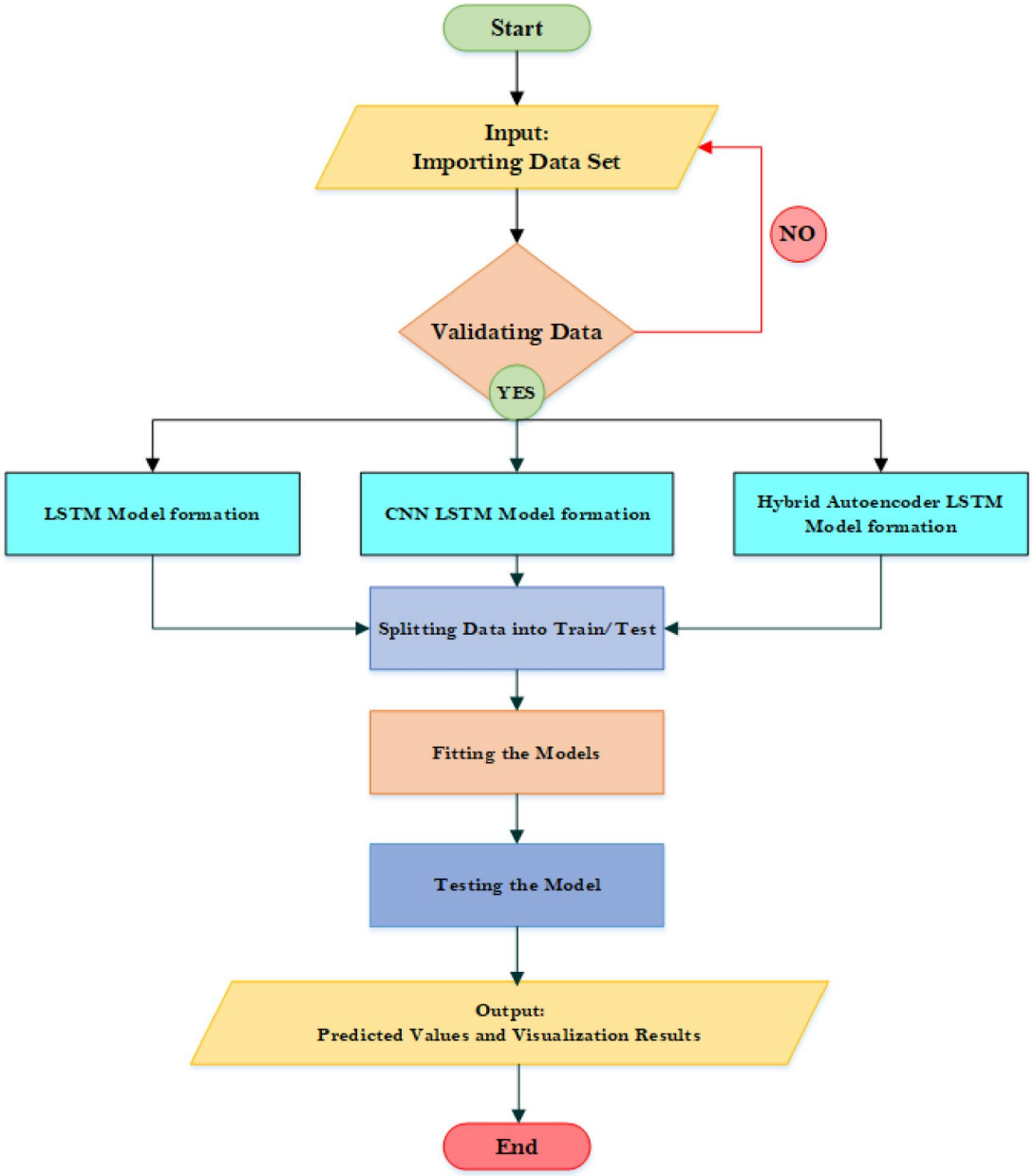

FIGURE 1 Proposed methodology flowchart to get final visualisations from LSTM, CNN LSTM and autoencoder LSTM.

RMSE and MAE values when applied to real-time solar farm data. Furthermore, the predictions obtained through autoencoder LSTM demonstrate higher accuracy compared to the CNN LSTM and LSTM model.

2.1 | Functional process of LSTM

A RNN unit has a type LSTM cell, its purpose is to control enduring dependencies in data sequences. It consists of several interconnected components that enable selective information retention or forgetting in time. The fundamental design of a basic LSTM cell, depicted in Figure 2, includes three main elements: the gate of input, the gate of forget, and the gate of output. These gates are responsible for regulating the flow of information inside the cell. Furthermore, there exists a memory cell that consistently refreshes and stores the data [8].

2.1.1 | Input gate

The input gate serves the purpose of determining the optimal extent of fresh data to be included within the cell of memory. By thinking about the input at present stage and the preceding state of hidden, it employs an activated function of sigmoid. This gate plays a decisive role in choosing the essential components of the input that necessitate remembrance and transfer to the memory cell.

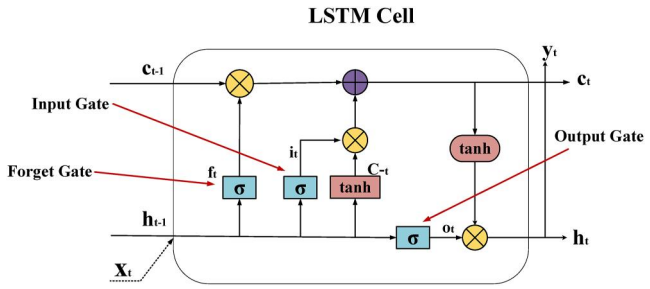

FIGURE 2 Long short-term memory cell structure.

2.1.2 | Forget gate

The gate of forget function is to control which data has to be eliminated from the memory cell. It takes both the present input and the preceding hidden state as inputs and employs a sigmoid activation function. The previous memory state of a cell is subsequently multiplied element-wise with the result of the forget gate, enabling the LSTM to intentionally disregard insignificant information.

2.1.3 | Memory cell

The memory cell is responsible for storing information persistently. It receives input from both the input plus forget gate. The input gate selects the fresh data that will be incorporated into the cell of memory, while the gate of forgotten regulates whether information ought to be deleted. Additionally, the memory cell possesses a self-loop connection, enabling it to maintain its previous state.

2.1.4 | Output gate

The output gate is responsible for determining the quantity of data from the cell of memory that must be conveyed to the subsequent state of hidden. It receives the input that is present and the preceding state of hidden as inputs, employs an activated function of sigmoid, and generates LSTM cell output. Moreover, a tanh function of activation is used to the final result in order to compress the values between −1 and 1.

The combination of these constituents enables the LSTM cell to selectively update the memory, retain vital information, discard unnecessary data, and generate outputs. By the incorporation of a separate memory cell and the control of information flow through gates, LSTMs excel at capturing enduring relationships in sequential data.

2.2 | Mathematical expression of LSTM

Three gates make up the LSTM cell structure: the forget gate, input gate, and output gates, controls the flow of information within the LSTM cell. Here, we provide a professional explanation of the equations mentioned in the research paper [14].

2.2.1 | Forget gate

Selecting whether data from the hidden state (h_{t-1}) of the previous time step and input at current (x_t) should be ignored is a crucial decision made by the gate of forget. To compute it, one uses the weighted summation of the inputs (W_f) and the function of sigmoid (σ), as shown in Equation (1):

$$f_t = \sigma\left\{W_f\left(h_{t-1}, x_t\right)\right\} \tag{1}$$

Here σ is the sigma function, weighted W_f sum of the inputs in the gate of forget, h_{t-1} is earlier step's time in the state of hidden and x_t is the present input.

2.2.2 | Input gate

Which essentials would be included into the present state of cell (f_t) is decided by the input gate. It consists of two parts. First, the gate layer of input, calculated using the function of sigmoid, selects the values that need to be updated. Second, the tanh layer produces new candidate (C'_t) values which might be appended to the state of cell. Equations (2) as well as (3) reflect the parameters of this gate:

$$I_t = \sigma\left\{W_i\left(h_{t-1}, x_t\right)\right\} \tag{2}$$

$$C'_t = \tanh\left\{W_c * \left(h_{t-1}, x_t\right)\right\} \tag{3}$$

2.2.3 | Cell state update

The state of cell (C_t) is modified considering the outputs from gate of forget (f_t), the earlier state of cell (C_{t-1}), the input gates (I_t), and the candidate cell states (C'_t). Equation (4) describes this update process:

$$C_t = \left(f_t * C_{t-1}\right) + C_t * C'_t \tag{4}$$

2.2.4 | Hidden state calculation

The state of hidden (h_t) is identified by multiplication between the output gate (O_t) and the present cell states (C_t) following its passage through the function of activation σ. Equation (5) represents this calculation:

$$O_t = \sigma\left\{W_o * \left(h_{t-1}, x_t\right)\right\} \tag{5}$$

$$h_t = O_t * \tanh\left(C_t\right) \tag{6}$$

where (W_f, W_i, W_c, W_o) are recurrent weights. Input, hidden, and state of cell at step t time are denoted by x_t, h_t and C_t, respectively. At step of time $t-1$, the hidden and cell state are h_{t-1} and C_{t-1}, respectively and sigmoid activation is σ.

The function sigmoid is represented by σ in all of the aforementioned equations. The input gate is represented by I_t, the gate of forgotten is denoted by f_t, the gate of output is represented by O_t, x_t represents the input for this step of time. The hidden state at this step of time is represented by h_t, C_t represents the current cell state, C'_t denotes the candidate state of cell at step (t) time, and C_{t-1} shows here the previous state of the cell. The equations outline the computations involved in updating the cell state's also generating the state of hidden in LSTM cell.

2.3 | Functional process of CNN LSTM

CNNs emphasise the structure of CNNs, which usually consists of an input layer, convolutional layer, pooling layer, fully connected layer, and output layer, for the direct detection of visual patterns in changing pixel pictures. The CNN LSTM model as shown in Figure 3, combines LSTM layers for sequence prediction with CNN layers for feature extraction. Applications for this approach include activity detection, labelling of images and videos, prediction in time series visually, and producing textual annotations from image sequences. An input layer for feature extraction and LSTM layers for modelling temporal dependencies, which help with sequence prediction are the first two components of the CNN LSTM architecture. With the CNN component extracting spatial characteristics and the LSTM component concentrating on modelling temporal patterns in the data, it provides an efficient way to handle spatial and temporal relationships in sequential data, such as video or time-series data [13]. CNN LSTM is useful in predicting time series data with complicated correlations because it is well-suited for jobs where both spatial and temporal patterns are important. Its shortcomings, however, become apparent when working with data that lacks meaningful spatial patterns. Autoencoder LSTM, which excels in dimensionality reduction, feature extraction, denoising, anomaly detection, and data reconstruction, steps in to help in these situations.

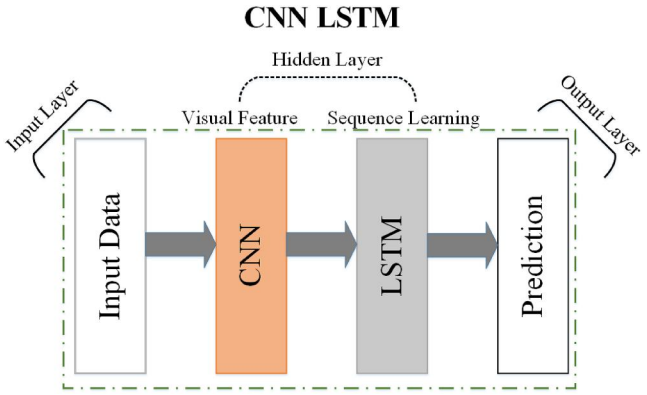

FIGURE 3 Structure of CNN LSTM.

2.4 | Functional process of autoencoder LSTM

Similarly, an autoencoder LSTM combines the idea of autoencoders and LSTM networks shown in Figure 4. A particular type of neural network known as autoencoder, which is instructed to reconstruct the input data, essentially learning a compressed form or 'encoding' of the input. By incorporating LSTM cells into an autoencoder architecture, can capture temporal dependencies and generate meaningful illustrations for sequential data [30].

The working of an autoencoder LSTM can be summed up in the steps below:

2.4.1 | Encoding

The LSTM encoder receives an input sequence. The LSTM cells in the encoder process the sequential data, capturing the temporal dependencies and generating a compressed representation called the encoding. The encoding typically has a lower dimensionality than the input sequence, enabling efficient representation of the data.

2.4.2 | Decoding

The encoding is then passed through the LSTM decoder. By producing an output sequence, the decoder of LSTM cells recreates the input sequence in original. Decoder learns to generate the output sequence by kept error during reconstruction as small as possible between the input's original version and the output's reconstruction.

2.4.3 | Training

The autoencoder LSTM is trained using a dataset that consists of input sequences. The objective is to reduce the difference between the input and their reconstructed outputs. Typically, this is accomplished by employing a function of loss like MSE

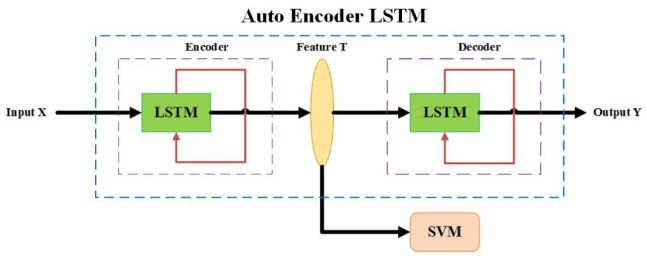

FIGURE 4 Structure of autoencoder LSTM.

aiming to reducing the dissimilarity between the original and recreated data.

2.4.4 | Compression and reconstruction

Once the autoencoder LSTM is trained, it can be used for compression as well as for reconstruction tasks. Given a new sequence of input, the encoder generates the compressed representation (encoding), and decoding recreates the initial sequence from the encoding. This allows the model to compress the input string into a shape of lower-dimensional, then recreate it with minimal loss.

By combining the capabilities of LSTM model for capturing dependencies with compression abilities of autoencoders, autoencoder LSTM models are well-suited for tasks for example, sequence forecasting, anomaly detection, and feature extraction from sequential data. The model learns to extract related information from the input sequence, capture its underlying patterns, and reconstruct it accurately.

2.5 | Mathematical expression of autoencoder LSTM

Typically, features are extracted using the autoencoder. $X = \{x_1, x_2, \ldots, x_k\}$, where $x_i \in R^d$ is an original input sequence of data. The formula f is used to determine the unique arrangement of the initial data. T stands for the sequence that defines the first sequence is x and is described as $T = \{t_1, t_2, \ldots, t_k\}$, whereas $t_i \in R^l$. The encoder output's is used as the decoder inputs. In accord with the characteristic T sequence, the decoder recreates the source data. The data that was rebuilt, $Y = \{y_1, y_2, \ldots, y_k\}$, where $y_i \in R^d$. Decoding is done to check the validity of the features that were extracted. The encoder is simply used by us to obtain the original data's properties once the autoencoder's training is complete so as to improve the data's internal structure. The Equations (7) and (8) for encoding and decoding are as follows [29]:

$$t_i = f\left(w_t \cdot x_i + b_t\right) \tag{7}$$

$$y_i = g\left(w_y \cdot t_i + b_y\right) \tag{8}$$

where w_t, w_y are weights, b_t, b_y are biases and sigmoid functions are represented by $f(\cdot)$ and $g(\cdot)$. The selection of weights and biases involves a training process. These model parameters are initialised with small random values. During training, the model performs forward passes, which include computing weighted sums of inputs, adding biases, and applying activation functions. Then the model's performance is evaluated using a loss function that measures the discrepancy between predicted and true values. Backpropagation is used to compute gradients of the loss with respect to weights and biases, which guide the model in adjusting these parameters to minimise the loss. Optimisation algorithms, such as stochastic gradient descent (SGD), are employed to iteratively update the weights and biases. This process is repeated for multiple epochs on the training data, allowing the model to learn the optimal parameter values. The model's performance is then validated and tested on separate datasets to ensure its generalisation capabilities [30]. Furthermore, after obtaining the best results, we save the weights and biases values for the future use, which automatically saves us time.

In an autoencoder, the working begins with the computation of the hidden state f_t using the first equation. It combines the input x_t, additional information z_t, and h_{t-1} is previous hidden state through a weighted sum, followed by the sigmoid function to introduce non-linearity. The equation second calculates the gate of input i_t by computing a weighted total of the inputs plus and state of previous hidden, further processed by the function of sigmoid. Afterwards, the candidate cell state C_t is gotten through a weighted sum of the inputs, and the earlier state of hidden, followed by tangent function of hyperbolic.

To update state C_t cell on step t time, Equation (3) combines the previous cell state C_{t-1} with state C'_t cell depending on the values of the forget f_t gate and the input i_t gate. The forget gate determines the retention of information from the previous cell state, while the input gate regulates the contribution of the candidate cell state. The output gate o_t is calculated in the Equation (5) using a weighted sum of inputs and the previous hidden state, passed through the function of sigmoid.

$$f_t = \sigma\left(w_{f1} \cdot x_t + w_{f2} \cdot z_t + wf_3 \cdot h_{t-1} + b_f\right) \tag{9}$$

$$i_t = \sigma\left(w_{i1} \cdot x_t + w_{i2} \cdot z_t + w_{i3} \cdot h_{t-1} + b_i\right) \tag{10}$$

$$C'_t = \tanh(w_{c1} \cdot x_t + w_{c2} \cdot z_t + w_{c3} \cdot h_{t-1} + b_c) \tag{11}$$

$$C_t = f_t \cdot C_{t-1} + i_t \cdot C'_t \tag{12}$$

C_t to obtain the hidden h_t state. In term of multiplication allows the selective output from the cell state, while tangent function of hyperbolic transforms result to form the final state of hidden. These equations collectively enable the autoencoder to encode and decode data, effectively compressing and reconstructing input information.

$$o_t = \sigma\left(w_{o1} \,.\, x_t + w_{o2} \,.\, z_t + w_{o3} \,.\, h_{t-1} + b_o\right) \tag{13}$$

$$h_t = o_t \,.\, \tanh\left(C_t\right) \tag{14}$$

z_t is a representation of the properties of data on both upstream and downstream traffic moves. Where recurrent weights are represented by (W_f, W_i, W_c, W_o) and (b_f, b_i, b_c, b_o) are biases. The input data for the forgotten gate encompasses three components: the existing input x_t, characteristics of both the previous and next steps z_t, also previous unit state h_{t-1}. C_t and C_{t-1} denote the cell states at time step t and $t-1$, correspondingly. The function of activation is used as the sigmoid

function, often represented as σ. The input data of output gate is comparable to the forgot gate. The information that should be output is chosen using the output gate. Finally, tanh processes the cell state and multiplies it by the output of the output gate.

We provide an enhanced model called autoencoder LSTM in our suggested framework, which is critical in forecasting three critical solar power generation parameters: 'Daily power generation', 'Maximum grid-connected power generation', and 'Radiance'. Figure 4 illustrates this model, which combines the memory capacities of LSTM networks with feature's extraction abilities of autoencoders. By efficiently comprehending the complex periodic patterns and present correlations in generating data of solar power, it seeks to improve forecast accuracy. The procedure consists of a number of steps: first, the raw data of solar power must be prepared; next, an autoencoder must be used to extract important features and compress the data; finally, the LSTM component must be used to apply this compressed representation in order to capture temporal correlations. The autoencoder LSTM is a reliable method for accurate power prediction because it can overcome the difficulties that regular LSTMs face in learning temporal relationships between sequences. The proposed model outperforms LSTM model and also CNN LSTM model in capturing temporal relationships and becomes trained at predicting future solar generation values through training on previous data. Section 4 delves deeper into this enhanced performance, emphasising the autoencoder LSTM model's efficacy in contrast to other models such as CNN LSTM.

3 | CASE STUDY

3.1 | Solar plant's structure

The Sapphire Solar Power Plant is a 100 MW solar power plant located in Chakwal, Punjab, Pakistan. It was developed by the Sapphire Group, a leading Pakistani conglomerate involved in textile manufacturing, power generation, and real estate. The solar power plant covers an area of approximately 650 acres and is equipped with over 400,000 solar panels. It is connected to the national grid through a 132 kV transmission line. The Sapphire Solar Power Plant began commercial operation in April 2018, and since then, it has been generating clean, renewable energy to satisfy Pakistan's expanding energy requirements. The plant is expected to generate approximately 165 GWh of electricity annually, which will help to reduce the country's reliance on fossil fuels and support its efforts to combat climate change. Constructing the Sapphire Solar Power Station was a significant milestone for the renewable energy sector in Pakistan, and it has helped to illustrate the viability of large-scale solar power projects in the country.

Figure 5 shows the structure of solar plant from where the data is collected. The single line diagram (SLD) of a solar power plant, containing 255-W solar panels, direct current (DC) to DC converters, DC to alternating current (AC) converters, a step-up transformer (32–132 kV), switchgear, and connections to domestic and industrial loads, provides a simplified graphical representation of the plant's structure. It illustrates the main parts of the solar power system and how they are connected. Solar panels, arranged in an array, serve as the primary source of power generation. DC to DC converters optimise the direct current output, while DC to AC converters convert it into alternating current. The step-up transformer elevates the voltage for efficient power transmission, and switchgear ensures system protection and control. Domestic and industrial loads represent the consumers of the generated electricity. The SLD offers a concise, high-level overview, making it an essential reference tool in the solar power plant's operation and maintenance.

3.2 | Installed equipment details at solar plant

Detailed information of the installed equipment is expressed as follows and also given in Table 1.

Solar Panels: More than 400,000 of 255-W solar panels have been installed at the power plant. The solar panels are manufactured by Trina Solar, a leading solar panel manufacturer based in China.

Inverters: The plant makes use of central inverters made by renowned Chinese solar inverter maker Sungrow. The solar panels' DC power is converted into grid-ready AC power by the inverters.

Mounting Structures: Solar panels are mounted on fixed-tilt mounting structures, which are designed to optimise the angle of the panels for maximum energy production. One of the top manufacturers of solar tracking technologies, Array Technologies, makes the mounting frameworks.

Transformers: Step-up transformers are used in the power plant to increase the voltage of solar energy before it is sent into the grid. Siemens, a top supplier of electrical equipment and facilities, makes the transformers.

Switchgear: Power plant's switchgear is designed to protect the electrical components and guarantee reliable, safe operation. ABB, a top supplier of technology in power, makes the switchgear.

Monitoring and Control System: The power plant has an advanced monitoring and control system that enables operators to keep an eye on equipment performance remotely and maximise energy production. Leader in information and communications technology solutions, Huawei, provides the monitoring and control solution.

3.3 | Data analysis

The dataset for SEVs comprises two categories of variables within the 100 MW solar plant. In this simulation utilising deep learning algorithms, the independent variables under consideration are the Maximum grid connected power generation and Radiation, while the dependent variable being analysed is the Daily power generation.

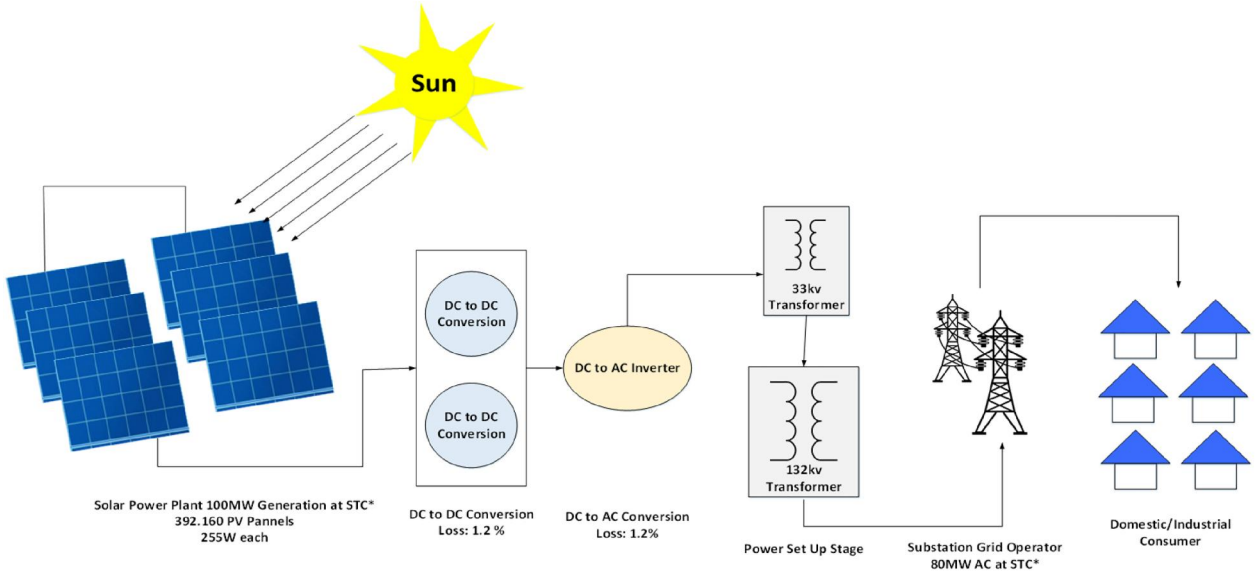

FIGURE 5 Single line diagram to express the structure of solar plant.

TABLE 1 Details of installed equipment.

Equipment detail's	No.	Units
Substation type	1	AIS
Capacity of plant	100	MW
Number of solar panels	400,000	255 Wp
Inverter	250	500 kW
Transformer (auxiliary)	120	0.315/33 kV
Feeder	20	132 kV loop collection system
Main transformer	02	132 kV–100 MVA
SVC (static var compensators)	02	−5~+15 MVAR

3.3.1 | Daily power generation

Daily power generation is a pivotal dependent variable in the realm of solar energy, often regarded as the plant's production parameter. It plays a central role in harnessing and optimising solar power plants, with improvements contingent on environmental influences and operational activities, encompassing maintenance. Typically falling within the range of 400–500 MW per day, the project consistently achieves its targeted power production. Daily power generation values are diligently monitored through energy metres and a Supervisory Control and Data Acquisition system, providing a dataset for simulation. This parameter quantifies the total electricity output from solar panels over a single day, measured in kilowatt-hours (kWh). It offers critical insights into a solar power plant's daily performance, considering factors, such as sunlight, panel efficiency, and weather-related fluctuations. Daily power generation is a pivotal metric for assessing the plant's efficiency and its capacity to meet energy demands while contributing to the renewable energy supply.

3.3.2 | Maximum grid connected power generation

Maximum grid-connected power generation serves as a critical independent variable in the realm of solar energy. It is non-dimensional and functions as a performance benchmark, often referred to as the quality factor or quality indicator for assessing solar plant efficiency. This metric plays a pivotal role in pinpointing the causes of energy losses and is instrumental in evaluating the effectiveness of solar energy in a given location. Measured in megawatts (MW), it represents the peak capacity at which a solar power plant can generate and supply electricity to the grid under ideal conditions. Grid operators and energy planners rely on this parameter to understand the plant's maximum potential contribution to the electrical grid. It considers factors such as solar panel capacity, efficiency, and sunlight intensity, facilitating effective grid management and enabling informed decisions about the integration of renewable energy into the grid. Additionally, it is a key metric used in performance evaluation and testing of solar plants, ensuring their quality and operational effectiveness.

3.3.3 | Radiance

In a solar power plant, radiation (MJ/m^2) is the term used to describe the quantity of solar energy incident or received on a certain surface area per unit of time. It is often measured in megajoules per square metre (MJ/m^2). It shows the energy flux density of sunlight falling on the solar panels or a specific section of the plant over a predetermined amount of time. Radiance considers variables including solar panel orientation, atmospheric conditions, and sunlight angle. This metric is crucial for evaluating the energy capture efficiency of the solar plant since it measures the intensity of incoming solar

radiation, which has an immediate effect on the plant's capacity to generate electricity. It is essential for maximising solar panel alignment and installation in order to improve energy absorption and plant performance as a whole.

A histogram is a helpful tool for analysing the properties of a dataset because it provides insights into the shape, centre, and spread of the data. Alternatively put, a histogram displays the distribution of the details. It may reveal unusual traits, compute statistical measures, such as the median, mean, and standard deviation, find patterns in the data, and show outliers or unusual qualities. As a whole, a histogram provides an easy-to-understand representation of the distribution of the data, which makes it simpler to compare various datasets and glean insights that may not be immediately evident from raw data. This is because a histogram organises the data in a way that is similar to a pie chart.

In Figure 6, histogram's 'Daily Power Generation' section shows unit distribution of everyday power from solar plants. A y-axis ranges from 0.00 to 0.067, signifying unit generation frequency. The number of units created is shown on the x-axis by 0–700,000 bins. Similarly, a histogram in which maximum grid-based power generating frequency about 0.00–0.06 and maximum grid-based power generating 0–100 MW values are separated into equivalent bins on the x-axis. It also depicts power generation values over time by counting maximum grid power values of production in every single bin and the y-axis are displayed with the frequencies. The 'Radiance' histogram features a 0.00–0.15 Y-axis and 0–30 X-axis. Radiance values are displayed on the X-axis at intervals of one width, the last break occurs between 29 and 30. The form of the histogram shows radiance value distribution. There tend to be low radiance scores when the histogram is inclined to the right than high ones when it is tilted to the left. A symmetrical histogram would display a uniform distribution of radiance.

Box plots shows a brief and useful approach of summarising huge datasets and acquiring knowledge about how they are distributed. Figure 7 illustrates the interquartile range (Q1–Q3), the median (Q2), and extremes or outliers results for three features obtained from a huge-scale power plant: Daily Generation, Highest Grid Connected Power Production, measured in MW, and Radiance. The vertical dimension of the container symbolises the central 50% of the information, while the lines at the ends stretch towards the smallest and largest values that lie across the initial and third quartiles, within 1.5 times that gap. Any points of data beyond this band be depicted as solitary dots or circular shapes, indicating potential noteworthy anomalies. Furthermore, it is crucial to avoid any form of plagiarism when reusing content.

The initial plot, 'Daily Power Generation in kWh', presents the range of 100,000–600,000 on the y-axis. The first quartile (Q1) falls between 330,000 and 450,000, indicating that the bottom 25% of the data resides within this interval. The second quartile (Q2) ranges among 450,000–500,000, indicating that the middle half (50%) of the data is contained within. The third quartile (Q3) ranges from 500,000 to 530,000, indicating that the upper 25% of the data lies within this interval. Lastly, the fourth quartile (Q4) ranges among 530,000–610,000, which indicates highest 1% of data is encompassed within.

The next box plot, 'Maximum Grid-Connected Power Generation in MW', shows the range between 10 and 90 MW on the y-axis. Q1 ranges from 60 to 70, indicating that the bottom 25% of the data resides within this interval. Q2 ranges from 70 to 73, indicating that the middle half (50%) of the data lies within this interval. Q3 ranges from 73 to 78, indicating that the upper 25% of the data lies within this range. Lastly, Q4 ranges among 78–88, which indicates that highest 1% of data is contained within.

The final box of plot, 'Radiance', shows the range between 5 and 30 MJ/m^2 on the y-axis. Q1 ranges from 14 to 20, indicating that the bottom 25% of the data resides within this interval. Q2 ranges from 20 to 22.5, indicating that the middle half (50%) of the data lies within this interval. Q3 ranges from 22.5 to 23.5, indicating that the upper 25% of the data resides within this interval. Lastly, Q4 ranges 23.5–27, which indicates that highest 1% of data is contained within, as depicted in Figure 7.

The heat map in Figure 8 illustrates the correlation of the three parameters in which three columns and three rows, with each cell representing the correlation coefficient between two parameters. The diagonal cells show the correlation of each parameter with itself, which is always 1. A more positive association is shown by higher numbers and lower numbers indicate a weaker negative correlation among the two variables. The values in the cells vary between 0 and 1. As an illustration, a positive correlation is denoted by a correlation factor of 1, a negative correlation is implied by a factor of −1, and no correlation is shown by a factor of 0. The range about correlation coefficients is represented by colour bar on the right side of the heat map. The colour bar has a range between 0.6 and 1.0, deeper hues correspond to higher positive correlation and lighter hues to lower positive correlation.

The findings obtained from the models are presented in graphical depiction form in the following Section 4.

4 | RESULTS AND DISCUSSION

This section presents the findings derived from analysing a year's worth of real-time data from a solar power plant, consisting of three essential parameters: 'daily power generation', 'maximum grid-connected power generation', and 'radiance'. Our objective was to develop ML models for future predictions based on this dataset. After an extensive review of the literature, we opted for the LSTM model due to its promising track record in similar applications. The LSTM model implementation yielded satisfactory results. However, in our pursuit of enhancing prediction accuracy, we introduced two additional models, namely the CNN LSTM and the autoencoder LSTM. The results are represented visually, and it is clear that the autoencoder LSTM model performed better than the CNN LSTM plus LSTM models, exhibiting decreased error rate and better forecasting accuracy.

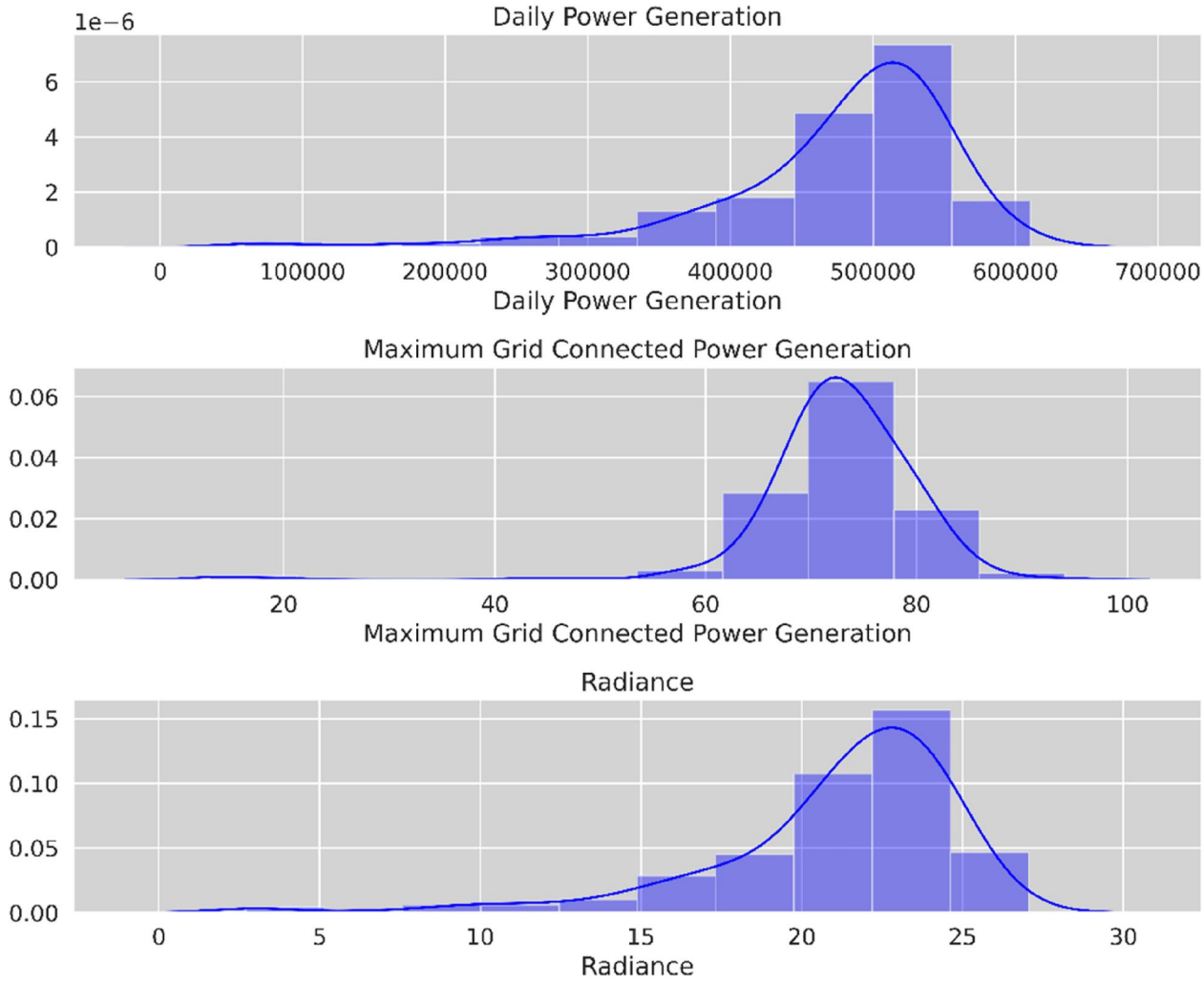

FIGURE 6 Analysis of solar plant parameters data through a histogram.

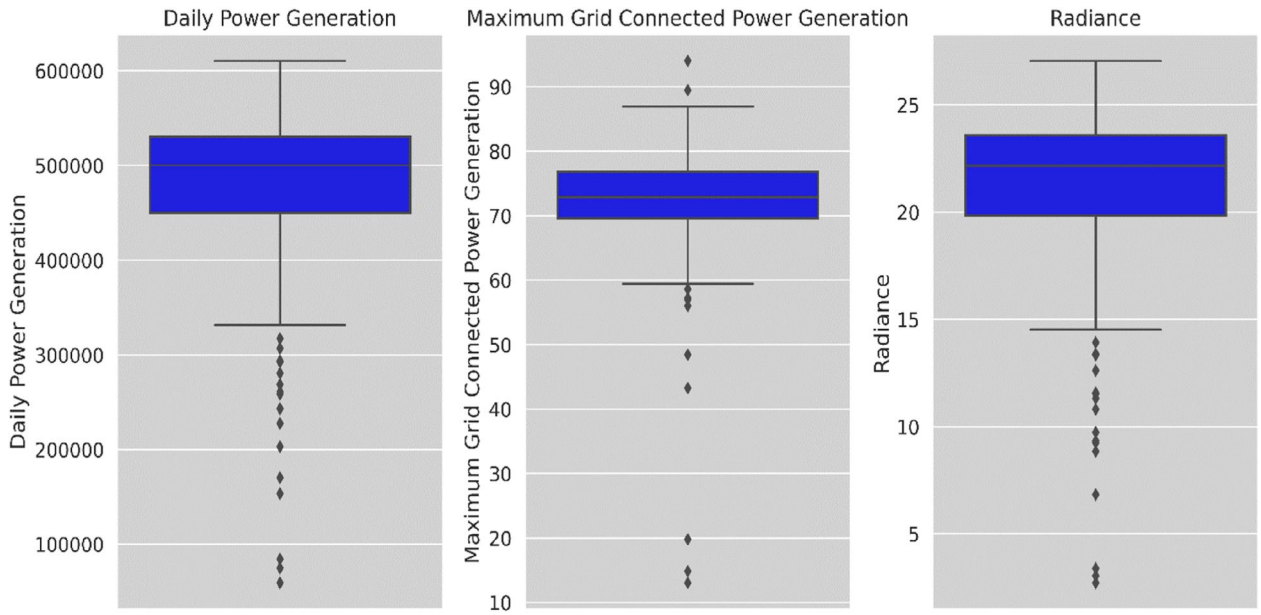

FIGURE 7 Analysis of solar plant parameters data through box plot.

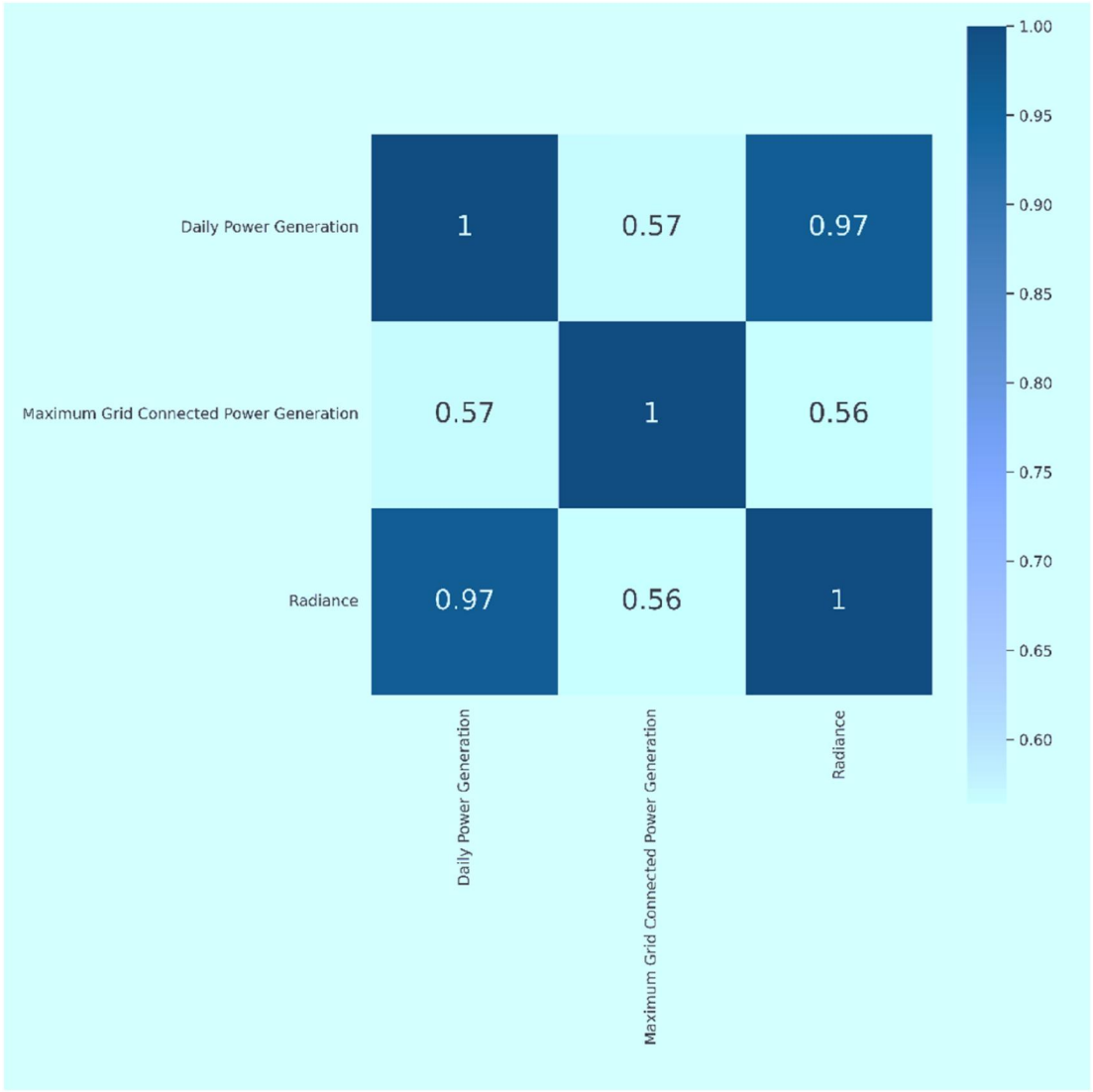

FIGURE 8 Analysis of solar plant parameters data through a heat map.

The practical applicability of parameters, such as daily power generation (kWh), grid-connected power generation (MW), and radiance (MJ/m^2) is of paramount importance in forecasting solar power plants. These parameters have multifaceted roles that significantly impact various aspects of solar energy production. Daily power generation (kWh) is instrumental in assessing plant performance, ensuring efficient maintenance, and estimating revenue, making it indispensable for plant operators and owners. Grid-connected power generation (MW) forecasts are crucial for grid stability, energy pricing, efficient grid management, and renewable energy integration, supporting sustainable energy practices. Radiance (MJ/m^2) is vital for estimating energy yield, performance monitoring, maintenance planning, and site suitability assessment, enhancing the economic viability and reliability of solar power projects. Together, these parameters contribute to optimising efficiency, sustainability, and reliability in solar energy generation. Furthermore, by encouraging the generation of cleaner energy and lowering dependency on fossil fuels, these models support sustainability objectives. Last but not least, their integration into smart grids improves overall grid performance, stability, and the effective use of renewable energy, all of which are in line with the larger objective of developing power systems that are more sustainable and efficient. This section explores the findings, showcasing the autoencoder LSTM model's noteworthy enhancements through tables and graphical displays.

Table 2 offers a detailed overview of a neural network model, shedding light on its architecture and parameter configuration. This model is composed of multiple layers, including both simple LSTM layers and more complex ones, each designed for specific data processing tasks. The output measurements produced by each of the layers are specified in the 'Output Shape' column. For instance, the first LSTM layer (lstm_115) yields outputs with a form of (None, 6, 10), meaning that it has a length of sequence 6 and a feature value of 10, and it provides results without a defined batch size. The output forms of the next two LSTM layers, lstm_116 and

TABLE 2 Step-by-step LSTM model sequence for prediction.

Layer (type)	Output shape	Param #
lstm_115 (LSTM)	(None, 6, 10)	530
lstm_116, lstm_116 (LSTM)	(None, 6, 8)	458
lstm_117 (LSTM)	(None, 1)	42
repeat_vector_31	(None, 1, 1)	0
lstm_118 (LSTM)	(None, 1, 10)	530
lstm_119 (LSTM)	(None, 1, 10)	890
dense_31 (dense)	(None, 1, 1)	18
Total params: 2468		
Trainable params: 2468		
Non-trainable params: 0		
None		
dict_keys (['loss', 'mse', 'mae', 'val_loss', 'val_mse', 'val_mae'])		

lstm_117, are (None, 4, 8) and (None, 1), respectively. The total amount of parameters that are trainable in each of the layers, including weights and biases, is shown in the 'Param #' column. In this particular model, lstm_115 has 530 variables; lstm_116 has 458 variables; lstm_117 has 42 variables; here repeat_vector_31, a repeating layer, has no variables; lstm_118 has 530 variables; lstm_119 has 890 variables; and dense_31 has 18 variables. With each variable selected to be trainable, the model has 2468 total trainable parameters. Additionally, Table 2 emphasises that this particular model does not contain any non-trainable variables. The dictionary keys 'loss', 'mse', 'mae', 'val_loss', 'val_mse', and 'val_mae' correspond to a variety of loss metrics used in the model's training and evaluation. The table also contains these dictionary keys. Metrics like MAE and MSE are essential for evaluating the performance of the model. The information presented in this table offers essential insights into the model's structure, layer configurations, parameter counts, and the various loss metrics available, contributing valuable information about the model's composition and its evaluation criteria.

Real-time data values for 1 year made up the dataset, utilises 80% for training purpose of both models and the outstanding 20% for testing or validation. The generated losses in terms of graphical visualisations are compared from the models.

In Figure 9(a), we can observe the loss values for the autoencoder LSTM, CNN LSTM, and LSTM models during a 100-epoch training process on the Daily Power Generation dataset. At the outset (Epoch 0), the autoencoder LSTM model exhibited a loss of 0.54054, signifying a relatively high starting point. Conversely, the CNN LSTM model started with an even higher loss of 0.97713, while the LSTM model had a moderate loss of 0.32687. As training progressed, by the 30th epoch, the autoencoder LSTM model had made significant improvements, achieving a notably lower loss of 0.02462, surpassing both the CNN LSTM (0.06694) and LSTM (0.09753) models. By the final epoch (Epoch 99), the autoencoder LSTM model achieved the least amount of loss at 0.02492, while the CNN LSTM model struggled with loss 0.03561, and the LSTM model settled at a loss 0.09752.

Similarly, in Figure 9(b), we explore the validation loss across 100 epochs for these three models on the Daily Power Generation dataset. At Epoch 0, the LSTM model started with a validation loss of 0.25755, whereas the initial losses of the autoencoder LSTM model and the CNN LSTM model were 0.44094 and 0.31631, respectively. Notably, by the 30th epoch, the LSTM model demonstrated consistent progress, reaching a validation loss of 0.09782. In contrast, the CNN LSTM model struggled with 0.04623 of loss, and the autoencoder LSTM model showed more promise at 0.02439. Throughout the training process, the autoencoder LSTM model reliably performed better than the other models, achieving the lowest validation loss by the final epoch (0.02444). In comparison, the CNN LSTM model had a higher loss of 0.03335, and the LSTM model settled at 0.09761 by the last epoch.

In summary, the autoencoder LSTM model consistently proved to be the most effective in capturing underlying patterns within the Daily Power Generation data, as evidenced by the loss and validation loss metrics, also reflected in Figure 9a,b.

In the context of Grid Connected Power Generation, an examination of loss values for LSTM, CNN LSTM, and autoencoder LSTM models across 100 training epochs, as illustrated in Figure 9(c), reveals interesting insights. At the initial epoch (Epoch 0), the LSTM model exhibited a starting loss of 0.21631, while the CNN LSTM and autoencoder LSTM models had substantially higher losses at 2.43105 and 0.49359, respectively. As the training advanced, all models consistently reduced their losses. By the 30th epoch, the autoencoder LSTM model stood out with an impressive loss of 0.00968, surpassing the CNN LSTM (0.03184) and LSTM (0.03864) models. Ultimately, by the 99th epoch, the autoencoder LSTM model achieved the lowest loss of 0.00972, showcasing its proficiency in capturing data patterns. In contrast, the CNN LSTM model and LSTM model concluded with losses of 0.02496 and 0.03872, respectively.

Similarly, in Figure 9(d), when evaluating the validation loss over 100 epochs for Grid Connected Power Generation, at Epoch 0 the LSTM model began with a loss of 0.17727, while the CNN LSTM and autoencoder LSTM models had slightly higher initial losses of 0.28154 and 0.42723, respectively. As training progressed, all three models consistently reduced their validation losses. By the 30th epoch, the LSTM model achieved 0.03867 of validation loss. In contrast, the CNN LSTM model exhibited a loss of 0.03945 at the same epoch, while the autoencoder LSTM model showcased remarkable performance with a substantially lower validation loss of 0.00967. This trend persisted throughout training, culminating in the autoencoder LSTM maintaining the lowest 0.0097 of validation loss by the final epoch (Epoch 99). In comparison, the CNN LSTM model achieved a validation loss (0.00928), and the LSTM model had a validation loss 0.03869.

These observations underscore the autoencoder LSTM model's higher performance in effectively capturing data

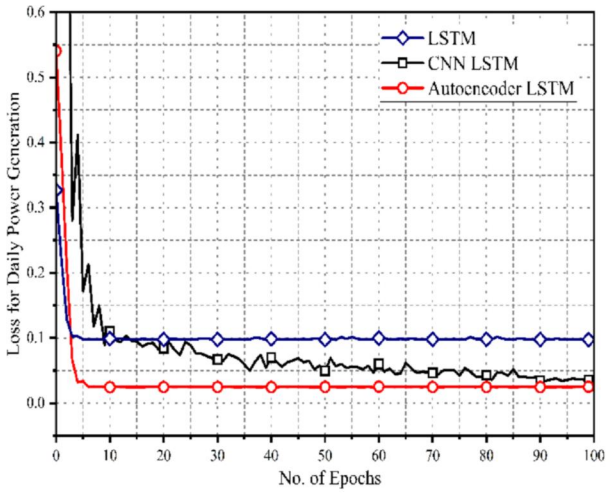

(a). Actual Loss of Daily Power Generation through LSTM, CNN LSTM, Autoencoder LSTM

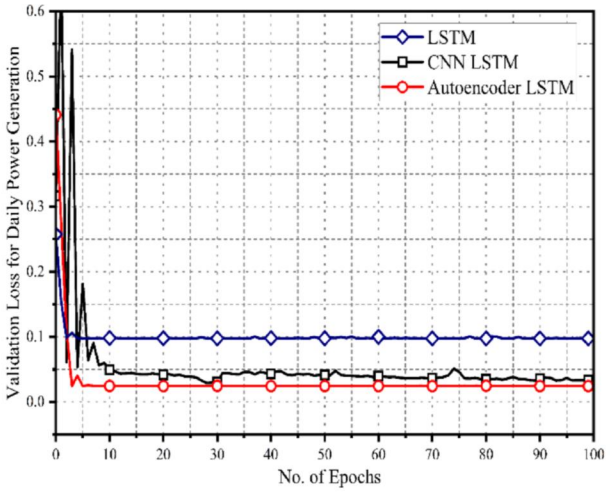

(b). Validation Loss of Daily Power Generation through LSTM, CNN LSTM, Autoencoder LSTM

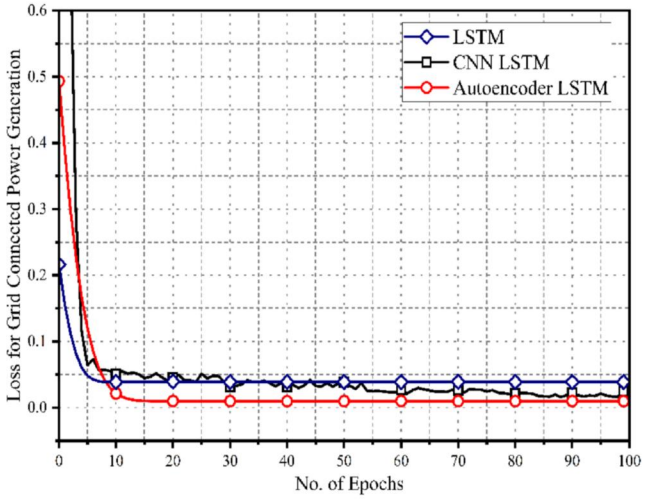

(c). Actual Loss of Grid Connected Power Generation through LSTM, CNN LSTM, Autoencoder LSTM

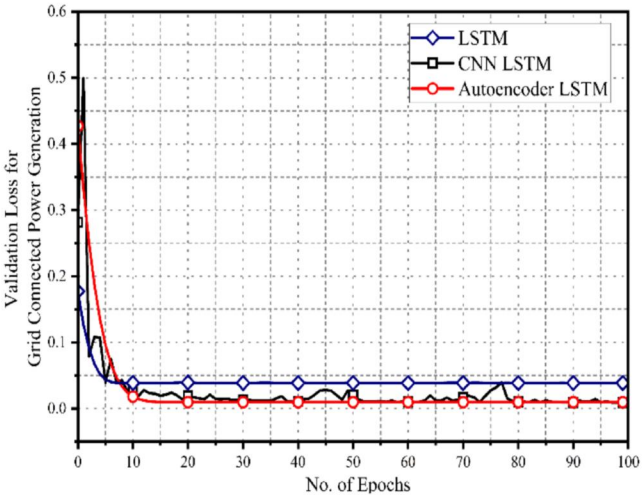

(d). Validation Loss of Grid Connected Power Generation through LSTM, CNN LSTM, Autoencoder LSTM

FIGURE 9 (a) Actual loss of daily power generation through LSTM, CNN LSTM and autoencoder LSTM. (b) Validation loss of daily power generation through LSTM, CNN LSTM and autoencoder LSTM. (c) Actual loss of grid connected power generation through LSTM, CNN LSTM and autoencoder LSTM. (d) Validation loss of grid connected power generation through LSTM, CNN LSTM, and autoencoder LSTM. (e) Actual loss of radiance through LSTM, CNN LSTM and autoencoder LSTM. (f) Validation loss of radiance through LSTM, CNN LSTM, and autoencoder LSTM.

patterns and minimising both training and validation loss compared to the other two models during the entire training process.

In Figure 9(e), a comprehensive analysis of loss values for the Radiance parameter across 100 training epochs in the LSTM, CNN LSTM, and autoencoder LSTM models reveals distinct trends. Initially, at Epoch 0, the LSTM model started with a loss of 0.23109, while the CNN LSTM and autoencoder LSTM models began with notably higher losses of 2.84988 and 0.54586, respectively. As the training progressed, all three models consistently reduced their losses. By the 30th epoch, the autoencoder LSTM model showcased remarkable performance with a significantly lower loss of 0.02484, outperforming both the CNN LSTM (0.05873) and LSTM (0.0706) models. Ultimately, by the 99th epoch, the autoencoder LSTM model maintained the lowermost loss at 0.02484, highlighting its effectiveness in capturing data patterns. In contrast, the CNN LSTM model achieved 0.05886 loss, and the LSTM model had loss 0.06595.

Likewise, in Figure 9(f), when examining the validation loss for the Radiance parameter over 100 epochs in the LSTM, CNN LSTM, and autoencoder LSTM models, discernible patterns emerge. At the beginning (Epoch 0), the LSTM model started with 0.09372 of validation loss, while the CNN LSTM

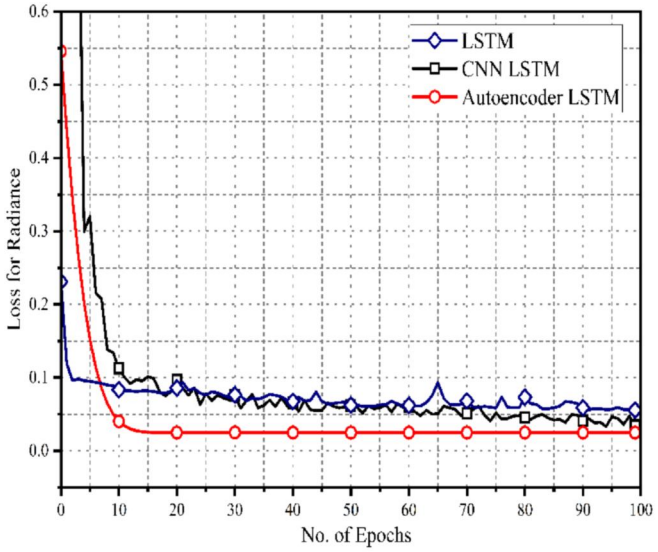

(e). Actual Loss of Radiance through LSTM, CNN LSTM, Autoencoder LSTM

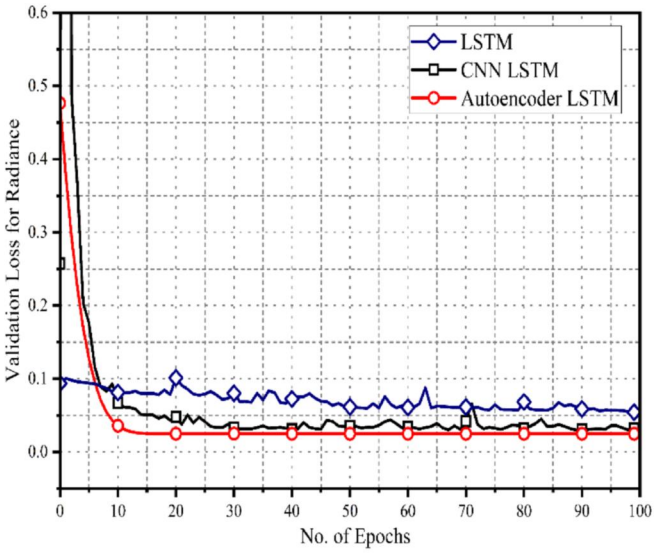

(f). Validation Loss of Radiance through LSTM, CNN LSTM, Autoencoder LSTM

FIGURE 9 (Continued)

and autoencoder LSTM models exhibited higher losses at 0.25752 and 0.47653, respectively. As the training continued, all models consistently reduced their losses. By the 30th epoch, the autoencoder LSTM model demonstrated impressive performance with a notably low validation loss of 0.02483, surpassing both the CNN LSTM (0.03335) and LSTM (0.08018) models. As the training concluded, the autoencoder LSTM maintained the lowest validation loss at 0.02482, underlining its effectiveness in capturing and generalising data patterns. In contrast, the CNN LSTM model achieved 0.03374 of validation loss, and the LSTM model ended with 0.06533 of validation loss.

These findings accentuate the outstanding performance of the autoencoder LSTM model, consistently achieving more effective minimisation of both loss and validation loss compared to the other two models throughout the training process for the Radiance parameter.

In Figure 10(a), the analysis of MAE for the Daily Power Generation parameter across 100 training epochs in the LSTM, CNN LSTM, and autoencoder LSTM models reveals compelling insights. At the beginning, during the first epoch, the LSTM model exhibited an MAE of 0.52936, while the CNN LSTM and autoencoder LSTM models had slightly higher MAEs of 0.91307 and 0.71785, respectively. However, as training progressed, all three models consistently reduced their MAE values. By the 50th epoch, the autoencoder LSTM model stood out with a significantly lower MAE of 0.10843, outperforming both the CNN LSTM (0.17757) and LSTM (0.22463) models. As the training process neared its conclusion, by the 99th epoch, the autoencoder LSTM model maintained a competitive MAE of 0.11735, highlighting its effectiveness in capturing data patterns for the Daily Power Generation parameter. In contrast, the CNN LSTM model achieved an MAE of 0.14016, and the LSTM model had an MAE of 0.22233.

Similarly, in Figure 10(b), the examination of the validation MAE for the Daily Power Generation parameter across 100 training epochs in the LSTM, CNN LSTM, and autoencoder LSTM models reveals distinct trends. During the first epoch, the LSTM model had an MAE of 0.4625, while the CNN LSTM and autoencoder LSTM models displayed slightly lower MAE values of 0.5009 and 0.64674, respectively. However, as training progressed, all three models consistently reduced their MAE values. By the 50th epoch, the autoencoder LSTM model exhibited remarkable performance with a notably lower MAE of 0.10805, outperforming both the CNN LSTM (0.12824) and LSTM (0.21886) models. Ultimately, by the 99th epoch, the autoencoder LSTM model maintained a competitive validation MAE of 0.11326, highlighting its effectiveness in capturing and generalising data patterns. In contrast, the CNN LSTM model achieved an MAE of 0.10664, and the LSTM model had an MAE of 0.2243.

These observations underscore the autoencoder LSTM model's superior performance in consistently reducing MAE and validation MAE more effectively than the other two models, particularly during the initial and middle phases of training for the Daily Power Generation parameter.

In Figure 10(c), the MAE for Grid Connected Power Generation parameter is examined across 100 training epochs in the LSTM, CNN LSTM, and autoencoder LSTM models. Initially, at the first epoch, the LSTM model had an MAE of 0.44178, while the CNN LSTM and autoencoder LSTM models had higher MAEs. As training progressed, all models consistently reduced their MAE values. By the 50th epoch, the

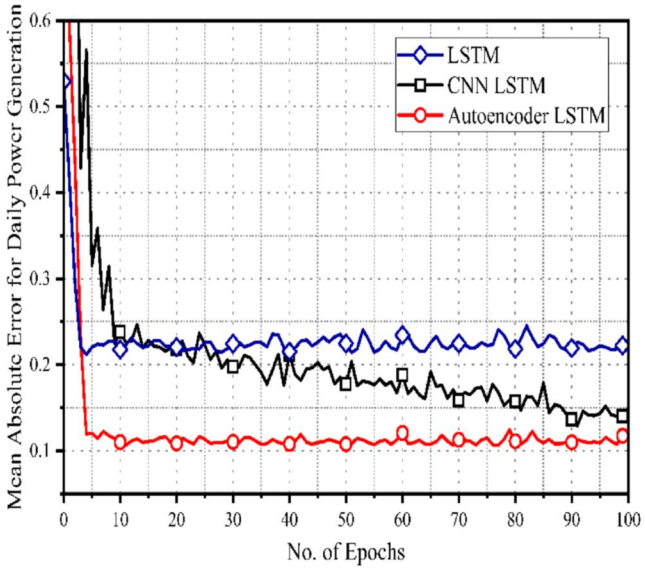

(a). MAE of Daily Power Generation through LSTM, CNN LSTM, Autoencoder LSTM

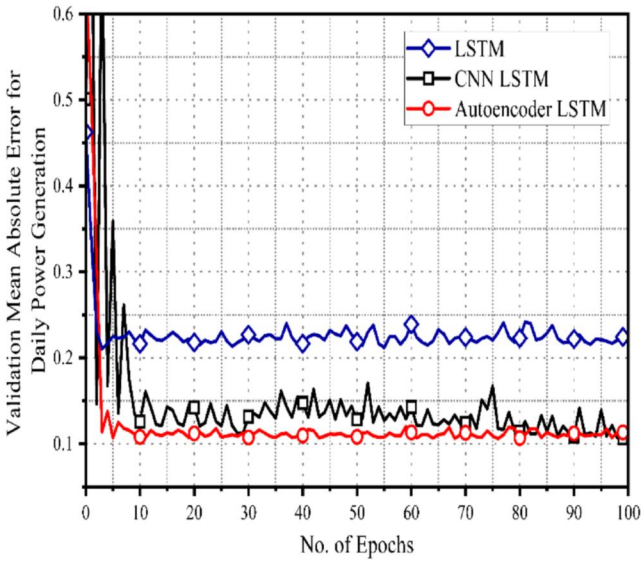

(b). Validation MAE of Daily Power Generation through LSTM, CNN LSTM, Autoencoder LSTM

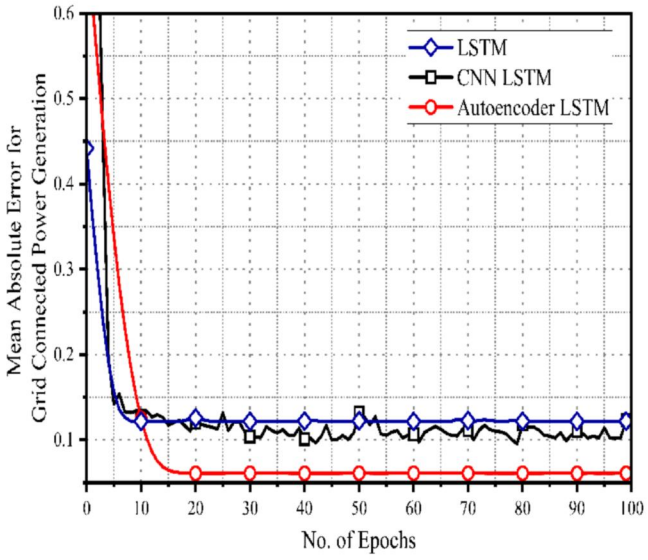

(c). MAE of Grid Connected Power Generation through LSTM, CNN LSTM, Autoencoder LSTM

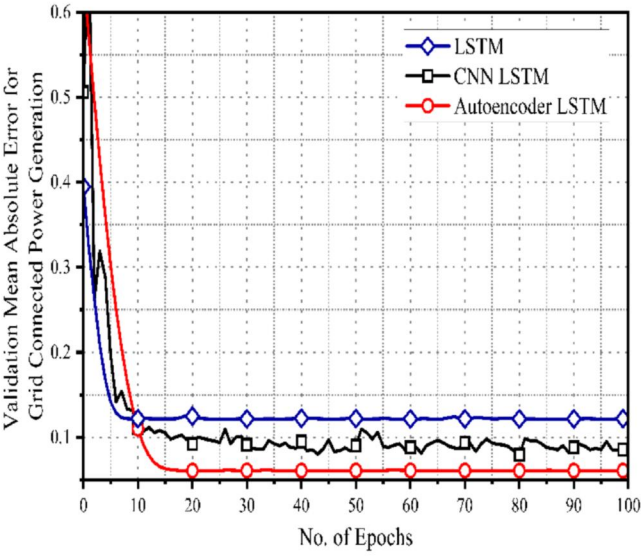

(d). Validation MAE of Grid Connected Power Generation through LSTM, CNN LSTM, Autoencoder LSTM

FIGURE 10 (a) MAE of daily power generation through LSTM, CNN LSTM and autoencoder LSTM. (b) Validation MAE of daily power generation through LSTM, CNN LSTM, and autoencoder LSTM. (c) MAE of grid connected power generation through LSTM, CNN LSTM and autoencoder LSTM. (d) Validation MAE of grid connected power generation through LSTM, CNN LSTM and autoencoder LSTM. (e) MAE of radiance through LSTM, CNN LSTM and autoencoder LSTM. (f) Validation MAE of radiance through LSTM, CNN LSTM and autoencoder LSTM.

autoencoder LSTM demonstrated superior performance with a substantially lower MAE of 0.10805. By the 99th epoch, the autoencoder LSTM maintained a highly competitive MAE of 0.06094, showcasing its data pattern generalisation capabilities. In contrast, the CNN LSTM and LSTM models had higher MAEs.

Similarly, in Figure 10(d), the validation MAE for the Grid Connected Power Generation parameter among the same models showed similar trends. The autoencoder LSTM model reliably outclassed the others, reaching the lowest validation MAE of 0.06082 by the 100th epoch, underlining its superior predictive accuracy. The CNN LSTM and LSTM models had higher validation MAEs.

These findings emphasise the autoencoder LSTM's consistent advantage in minimising both MAE and validation MAE, making it highly effective in delivering precise

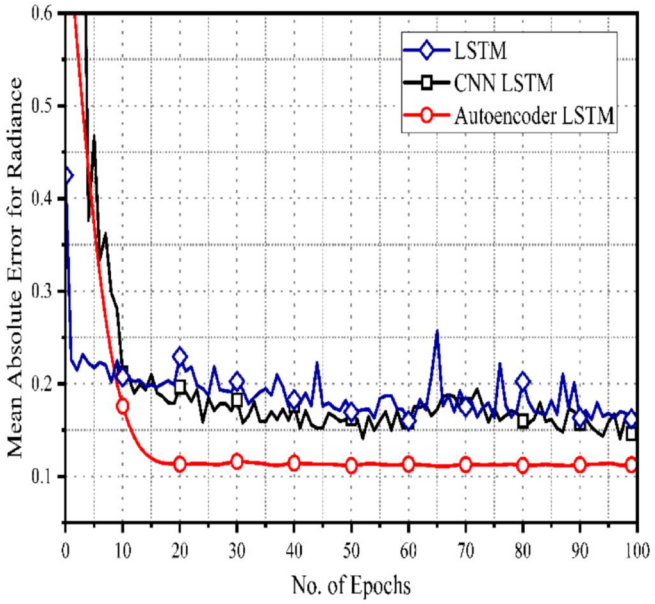

(e). MAE of Radiance through LSTM, CNN LSTM, Autoencoder LSTM

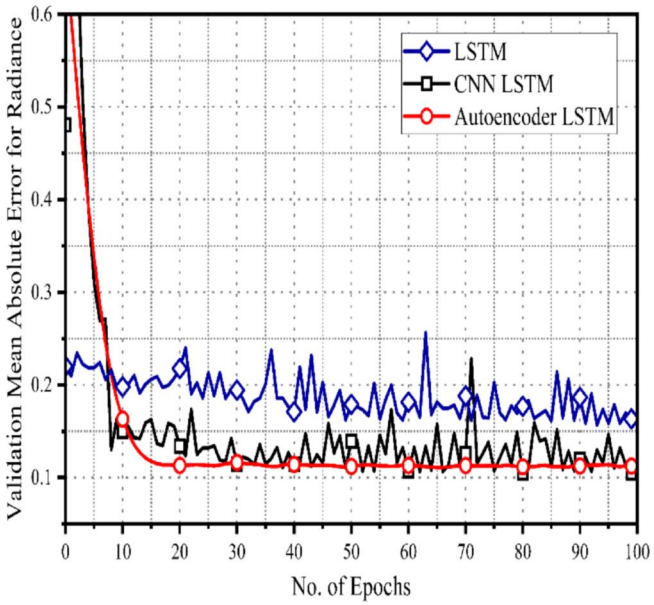

(f). Validation MAE of Radiance through LSTM, CNN LSTM, Autoencoder LSTM

FIGURE 10 (Continued)

predictions for the Grid Connected Generation parameter, with potential applications in real-world scenarios where accuracy is crucial.

Equation (15) is the formula to determine the MAE between the target variable's real and predicted scores is [29–31].

$$\mathrm{MAE} = \frac{1}{N}\sum_{n=1}^{N}\left|\overline{x_n} - x_n\right| \tag{15}$$

Where $\overline{x_n}$ represents the predicted value, x_n represents the real value and N is the total quantity of data.

In Figure 10(e), an analysis of the MAE for the Radiance parameter across 100 training epochs in the LSTM, CNN LSTM, and autoencoder LSTM models reveals noteworthy trends. Initially, at Epoch 0, the LSTM model exhibited an MAE of 0.42495, while the CNN LSTM and autoencoder LSTM models started with notably higher MAEs of 1.38619 and 0.72198, respectively. However, as the training progressed, all three models consistently reduced their MAE values. By the 50th epoch, the autoencoder LSTM model emerged as the standout performer, achieving a substantially lower MAE of 0.11313, surpassing both the CNN LSTM (0.16271) and LSTM (0.16933) models. Impressively, by the 99th epoch, the autoencoder LSTM maintained its impressive performance with a MAE of 0.11257, underscoring its effectiveness in capturing and generalising data patterns for the Radiance parameter. In contrast, the CNN LSTM model achieved an MAE of 0.14611, while the LSTM model had a MAE of 0.16188.

Similarly, in Figure 10(f), the validation MAE for the Radiance parameter over 100 training epochs is examined. Initially, during the first epoch, the LSTM model started with a validation MAE of 0.22013, while the CNN LSTM and autoencoder LSTM models had slightly higher validation MAEs of 0.48047 and 0.67314, respectively. However, as training continued, all three models consistently reduced their validation MAE values. By the 50th epoch, the autoencoder LSTM model showcased its superior performance with an impressively low validation MAE of 0.11301, outperforming both the CNN LSTM (0.13932) and LSTM (0.17891) models. By the 100th and final epoch, the autoencoder LSTM maintained its exceptional performance, achieving a validation MAE of 0.11238, the lowest among the three models. In contrast, the CNN LSTM model achieved a validation MAE of 0.10503, while the LSTM model had a validation MAE of 0.16331.

In summary, this analysis highlights the consistent advantage of the autoencoder LSTM model in reducing both MAE and validation MAE for the Radiance parameter, making it a robust choice for precise and accurate predictions. It showcases the autoencoder LSTM's potential for real-world applications where precision is of utmost importance.

Figure 11a,b provides an insightful analysis of MSE for the Daily Power Generation parameter throughout 100 training epochs in the LSTM, CNN LSTM, and autoencoder LSTM models, shedding light on their distinct performance trends. In Figure 11(a), the initial MSE values at Epoch 0 were relatively high, with the LSTM, CNN LSTM, and autoencoder LSTM models at 0.32687, 0.97713, and 0.54054, respectively. As training progressed, all models consistently reduced their MSE values. Notably, the autoencoder LSTM model exhibited

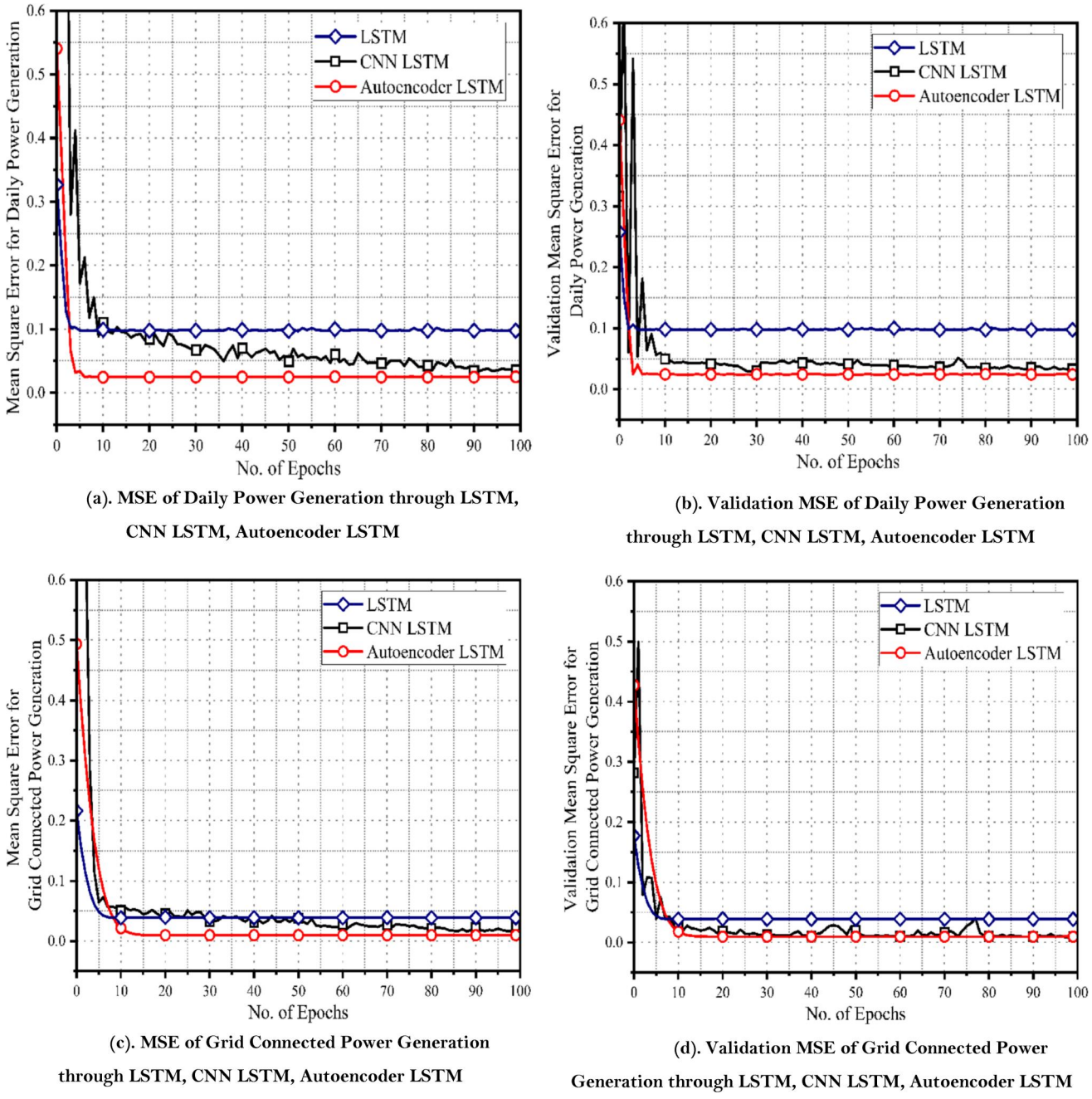

(a). MSE of Daily Power Generation through LSTM, CNN LSTM, Autoencoder LSTM

(b). Validation MSE of Daily Power Generation through LSTM, CNN LSTM, Autoencoder LSTM

(c). MSE of Grid Connected Power Generation through LSTM, CNN LSTM, Autoencoder LSTM

(d). Validation MSE of Grid Connected Power Generation through LSTM, CNN LSTM, Autoencoder LSTM

FIGURE 11 (a) MSE of daily power generation through LSTM, CNN LSTM, and autoencoder LSTM. (b) Validation MSE of daily power generation through LSTM, CNN LSTM, and autoencoder LSTM. (c) MSE of grid connected power generation through LSTM, CNN LSTM, and autoencoder LSTM. (d) Validation MSE of grid connected power generation through LSTM, CNN LSTM, and autoencoder LSTM. (e) MSE of radiance through LSTM, CNN LSTM, and autoencoder LSTM. (f) Validation MSE of radiance through LSTM, CNN LSTM and autoencoder LSTM.

remarkable proficiency, achieving an impressively low MSE of 0.02492 by the 90th epoch, outperforming the LSTM (MSE: 0.09752) and CNN LSTM (MSE: 0.03561). This highlights the autoencoder LSTM's potential for applications where precision and accuracy are critical.

Figure 11(b) delves into validation MSE for the Daily Power Generation parameter. At the outset, the LSTM model started with an MSE of 0.25755, while the CNN LSTM and autoencoder LSTM models had initial MSE values of 0.31631 and 0.44094. Similarly, as training progressed, all models consistently reduced their MSE values. By the 90th epoch, the autoencoder LSTM model achieved an exceptional validation MSE of 0.02444, surpassing the LSTM (MSE: 0.09761) and the CNN LSTM (MSE: 0.03335). This underscores the

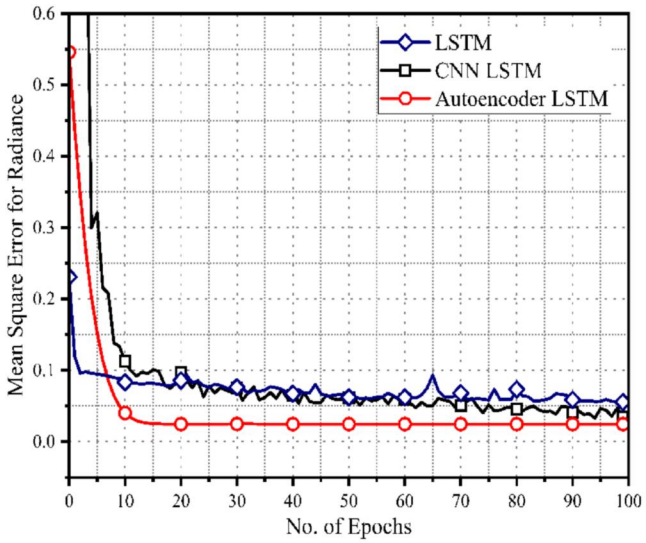

(e). MSE of Radiance through LSTM, CNN LSTM, Autoencoder LSTM

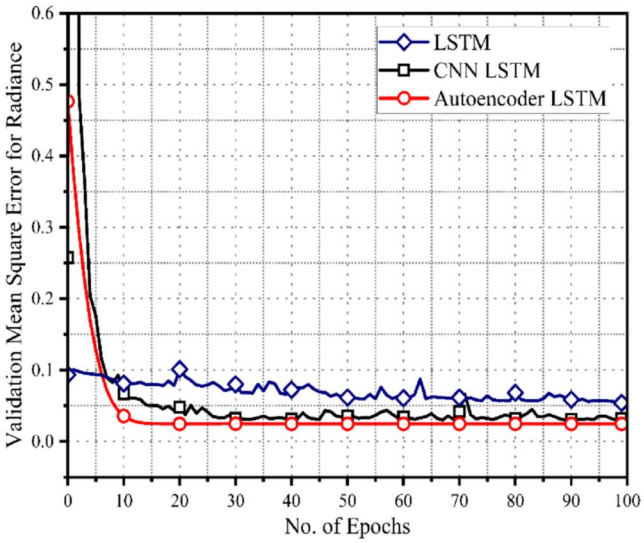

(f). Validation MSE of Radiance through LSTM, CNN LSTM, Autoencoder LSTM

FIGURE 11 (Continued)

autoencoder LSTM's superior performance in minimising validation MSE, especially considering both the initial and 90th epoch values. It indicates the autoencoder LSTM model's suitability for applications prioritising precision and reliability in modelling and forecasting the Daily Power Generation parameter.

In the same way, Equation (16) is the formula to determine the MSE between the target variable's real and predicted scores [29–31].

$$\mathrm{MSE} = \frac{1}{N}\sum_{n=1}^{N}\left(\overline{x_n} - x_n\right)^2 \tag{16}$$

where $\overline{x_n}$ represents the predicted value, x_n represents the real value and N is the total quantity of data.

In Figure 11c,d, an in-depth analysis of the MSE and validation MSE for the Grid Connected Power Generation parameter across 100 training epochs in LSTM, CNN LSTM, and autoencoder LSTM models uncovers noteworthy trends. Figure 11(c) shows that at the initial stage, during the first epoch, the LSTM model started with an MSE of 0.21631, while the CNN LSTM and autoencoder LSTM models began with relatively higher MSE values of 2.43105 and 0.49359, respectively. Nevertheless, as training proceeded, all three models consistently reduced their MSE values, indicating their effectiveness in learning from data patterns. By the 90th epoch, the autoencoder LSTM model impressively achieved an MSE of 0.00967, showcasing its exceptional ability to model the Grid Connected Power Generation parameter. In comparison, the LSTM model reached a MSE of 0.03874, and the CNN LSTM model exhibited a MSE of 0.02496. Similarly, in Figure 11(d), the evaluation of validation MSE reveals parallel trends. In the first epoch, the LSTM model had a validation MSE of 0.17727, slightly higher than the CNN LSTM (0.28154) and autoencoder LSTM (0.42723) models. As training progressed, all three models consistently reduced their validation MSE values, highlighting their capacity to capture data patterns effectively. By the 90th epoch, the autoencoder LSTM model achieved an impressive validation MSE of 0.00967, underlining its proficiency in modelling the Grid Connected Power Generation parameter. In comparison, the LSTM model had a validation MSE of 0.03867, and the CNN LSTM model exhibited a validation MSE of 0.00928.

In summary, the autoencoder LSTM model consistently excelled in minimising both MSE and validation MSE for the Grid Connected Power Generation parameter, from the initial values to the final epochs. This highlights its suitability for applications where precision and accuracy in modelling and forecasting are crucial.

Figure 11e,f presents a thorough analysis of the performance of LSTM, CNN LSTM, and autoencoder LSTM models in modelling the Radiance parameter over 100 training epochs, with a specific focus on MSE and validation MSE.

In Figure 11(e), the models' initial MSE values in the first epoch reflected their diverse starting points, with the autoencoder LSTM standing out by beginning with the lowest MSE of 0.54586. As the training progressed, the LSTM model showcased its learning capabilities, reaching an MSE of 0.05571 by the 90th epoch. The CNN LSTM displayed notable adaptability, achieving an MSE of 0.03486. However, the autoencoder LSTM consistently outperformed both by maintaining impressively low MSE throughout, settling at 0.02484 by the 90th epoch. This consistent superiority makes the autoencoder LSTM the ideal choice for precise Radiance parameter predictions. Similarly, in Figure 11(f), the validation MSE data revealed a similar trend. The autoencoder LSTM

TABLE 3 Comparison table between LSTM, CNN LSTM, and autoencoder LSTM results.

	LSTM			CNN LSTM			Autoencoder LSTM		
Parameter	**Loss**	**MAE**	**MSE**	**Loss**	**MAE**	**MSE**	**Loss**	**MAE**	**MSE**
Radiance	0.05571	0.16188	0.05571	0.03486	0.14611	0.03486	0.02484	0.11257	0.02484
Grid connection power generation	0.03872	0.12196	0.03872	0.02496	0.10265	0.02496	0.00972	0.06094	0.00972
Daily power generation	0.09752	0.22233	0.09752	0.03561	0.14016	0.03561	0.02492	0.11735	0.02492

started with the lowest validation MSE of 0.47653, again emphasising its ability to capture the Radiance parameter's patterns from the beginning. By the 90th epoch, the LSTM reached an MSE of 0.05427, while the autoencoder LSTM achieved an impressively low validation MSE of 0.02482. The CNN LSTM showed adaptability but fluctuation, concluding at an MSE of 0.03212. The autoencoder LSTM's consistency and lower MSE values establish it as the preferred model for accurate Radiance parameter predictions.

In summary, the autoencoder LSTM's remarkable ability to minimise both training and validation MSE underscores its suitability for applications requiring precise and reliable Radiance parameter forecasting.

Table 3 provides a comparison of the performance of different LSTM-based models, Simple LSTM, CNN LSTM and autoencoder LSTM, on three parameters: Radiance, Grid Connection Power Generation, and Daily Power Generation. The table includes the loss values, MAE, and MSE, for each model and parameter. For the parameter radiance, the Simple LSTM model has loss 0.05571 with an MAE of 0.16188 and an MSE of 0.05571 and CNN LSTM model has loss 0.03486 with an MAE of 0.14611 and an MSE of 0.03486. On the other hand, the autoencoder LSTM model attains a lower loss of 0.02484 with an MAE of 0.11257 and an MSE of 0.02484. Similarly, for the Grid Connection Power Generation parameter, the LSTM model has a loss of 0.03872 with an MAE of 0.12196 and MSE of 0.03872, where CNN LSTM model has loss 0.02496 with an MAE of 0.10265 and MSE 0.02496. However, the autoencoder LSTM model performs better with a lower loss of 0.00972, an MAE of 0.06094, and an MSE of 0.00972. Lastly, for the Daily Power Generation parameter, the Simple LSTM model and CNN LSTM has a loss of 0.09752 with an MAE of 0.22233, MSE of 0.09752 and has a loss of 0.03561 with an MAE of 0.14016 and an MSE of 0.03561 respectively. The autoencoder LSTM model attains a lower loss of 0.02492, an MAE of 0.11735, and an MSE of 0.02492. Overall, the table highlights the performance of the models on different parameters, with the autoencoder LSTM model consistently outperforming both the CNN LSTM and LSTM model in regards to lower loss, MAE, and MSE values.

Although our proposed autoencoder LSTM model has demonstrated impressive predictive precision concerning solar power parameters, the likelihood of its practical application is contingent on various determinants. Therefore, the potential implementation of the autoencoder LSTM model is closely linked to factors including the readiness of the industry, the availability of resources, and the effectiveness of knowledge transfer. A comprehensive evaluation of these elements will yield important information about the model's prospects for successful integration within the realm of solar plant operations. The implementation probability of the proposed autoencoder LSTM model for real-time grid management software development is highly favourable, given its proven proficiency in forecasting crucial parameters for efficient grid operations. With its adaptability to real-time data, customisation options, and continuous feedback capabilities, the model aligns well with the evolving needs of dynamic grid management, promising increased forecasting accuracy over time and substantial support for cost efficiency and renewable energy integration, thereby reinforcing its practicality in real-time grid management software development.

In addition, a close examination of each model's graphical representation shows plenty of resemblance, suggesting that the accuracy of data is higher than 95% and that none of the outliers have been found. These results provide even more evidence for the applicability and accuracy of the power plant data, offering a strong basis for further investigation and making decision.

Figure 12 presents a graphical representation of 'Daily Power Generation (kWh)' data over a year, where the y-axis spans between 200,000 and 700,000 units, and the x-axis indicates the days in number. It is clear that this graph allows us to easily assess the accuracy and performance of different ML models used for prediction. The more closely the test data and forecast data match, the more accurate the models are in predicting this parameter accurately.

Comparing the predictions from LSTM, CNN LSTM, and autoencoder LSTM models to the actual test data over a 60-day period, it becomes evident that autoencoder LSTM performs exceptionally well. Its predictions almost match the test data with only minor discrepancies. When these models are applied to forecast daily power generation over the next 10 months (300 days), autoencoder LSTM consistently outperforms the other two models. It exhibits the lowest prediction errors compared to the actual test data, indicating its superior accuracy in forecasting daily power generation for the upcoming year. CNN LSTM follows, showing better performance than the basic LSTM model. This suggests that the CNN LSTM model captures more intricate patterns and dependencies in the data compared to the simpler LSTM.

In summary, the analysis of Figure 12 concludes that the autoencoder LSTM model is the most accurate for predicting daily power generation over the next year, followed by the CNN LSTM model. The basic LSTM model falls behind in terms of predictive accuracy. This information holds significance for decision-making in the energy sector, as it can assist

stakeholders in making more informed choices regarding power generation and distribution.

Figure 13 indicates the parameter's range 'Grid Connected Power Generation', spanning from 40 to 100 kWh on the *y*-axis, whereas the days in number is displayed on the *x*-axis. By comparing the predicted data from the LSTM, CNN LSTM, and autoencoder LSTM models with the last test data from real 60-day, it is obvious that the autoencoder LSTM model's predictions closely align with the findings from tests, albeit very little discrepancies at some points. Following this comparison, the 'Grid Connected Power Generation' is manipulated with the subsequent 10 months (300 days), as illustrated in Figure 13. The test data graph represents the actual values of the parameter obtained from the plant of solar power, while the prediction graphs depict the estimated values generated by the LSTM, CNN LSTM, and autoencoder LSTM models. Comparing the test and prediction data graphs allows for assessing the models' performance and accuracy. Without a doubt, Figure 13 shows that the autoencoder LSTM model performs better than both the CNN LSTM and the LSTM model. This is because the model's predictions closely match the test data, showing very few deviations and a high level of accuracy in forecasting grid-connected power generation. The CNN LSTM model, although not as accurate as the autoencoder LSTM, still provides more reliable predictions compared to the basic LSTM model.

This representation suggests that leveraging more advanced techniques, such as autoencoder LSTM, can significantly enhance the precision of power generation predictions. Decision-makers in the energy sector can rely on these models, with a preference for autoencoder LSTM, to make informed choices and ensure more efficient grid-connected power generation and distribution.

In Figure 14, we can observe the representation of the 'Radiance' parameter, ranging from 0 to 35 MJ/m^2 on the *y*-axis, whereas the days in number is displayed on the *x*-axis. This figure visually depicts predictions for radiance levels over the next year, using three distinct models—LSTM, CNN LSTM, and autoencoder LSTM. These models are subsequently utilised to forecast 'Radiance' for the remaining 10 months, as illustrated in Figure 14. The test data graph reflects actual values obtained from a solar power plant, while the prediction graphs illustrate estimated values generated by the LSTM, CNN LSTM, and

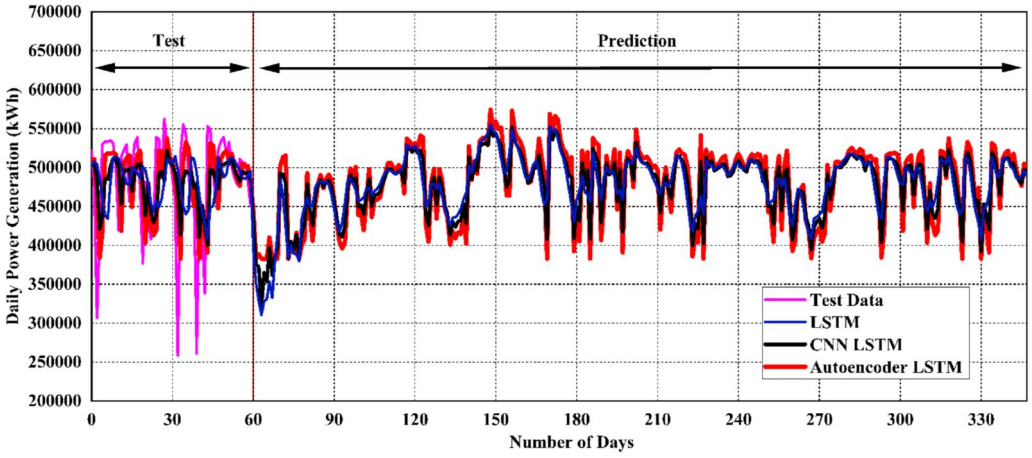

FIGURE 12 An analysis of LSTM, CNN LSTM, and autoencoder LSTM models for predicting solar plant daily power generation.

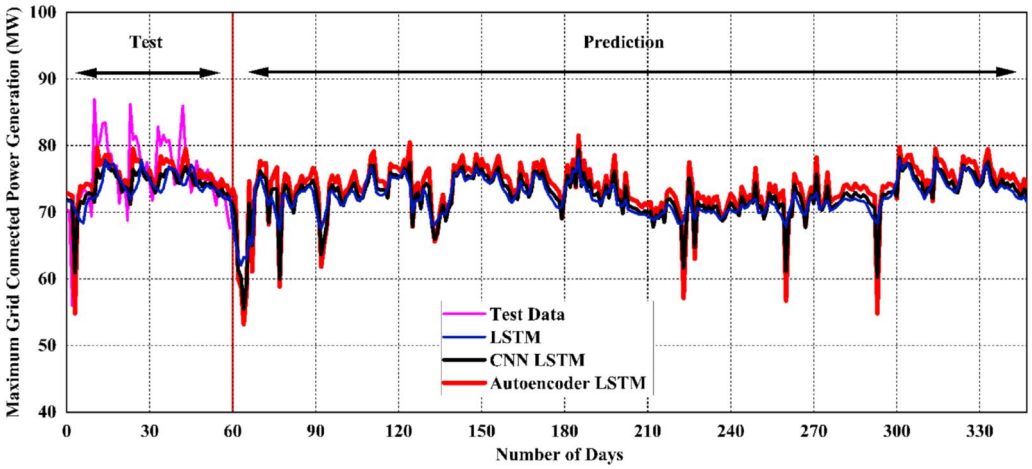

FIGURE 13 An analysis of LSTM, CNN LSTM, and autoencoder LSTM models for predicting solar plant grid connected power generation.

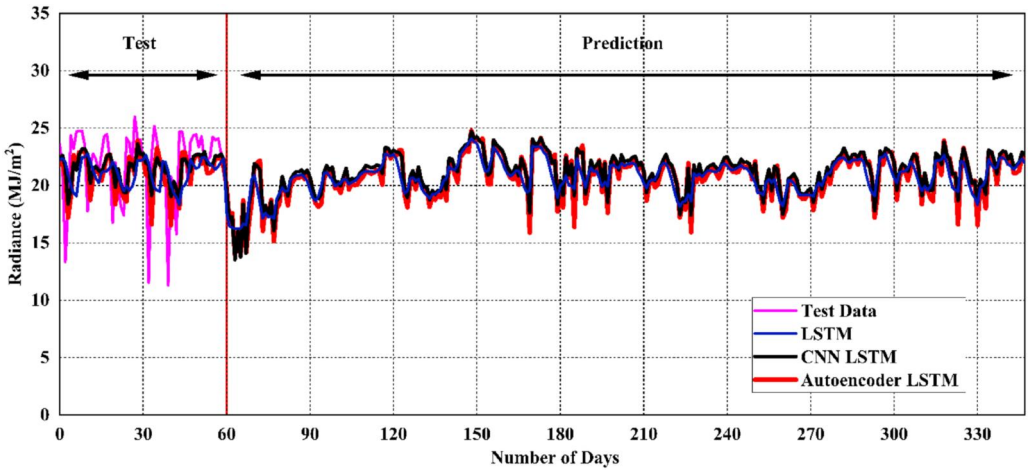

FIGURE 14 An analysis of LSTM, CNN LSTM, and autoencoder LSTM models for predicting solar plant radiance.

autoencoder LSTM models. The 60-day test data closely aligns with the predictions generated by the autoencoder LSTM model, with only minor variations at specific points. A detailed analysis of results reveals that the autoencoder LSTM reliably performs better then both the CNN LSTM and the basic LSTM model. The predictions made by the autoencoder LSTM closely match the test data, indicating a high level of accuracy in radiance forecasting. While some slight discrepancies exist, they are significantly fewer than those observed in the other models. The CNN LSTM model also demonstrates superior predictive capabilities compared to the basic LSTM, albeit falling slightly short of the accuracy achieved by the autoencoder LSTM. These findings underscore the significance of employing advanced techniques, particularly the autoencoder LSTM, for precise radiance predictions. This data is of great value to decision-makers in fields such as renewable energy, enabling them to make informed choices and enhance their planning for radiance-related applications in the upcoming year.

5 | CONCLUSION

In this comprehensive study, an in-depth analysis of daily power generation, grid-connected power generation, and radiance data from a solar plant over the course of a year was conducted. Three ML models, namely LSTM, CNN LSTM, and autoencoder LSTM, were carefully selected, extensively trained, and rigorously tested to make predictions about these crucial parameters. MAE and MSE were employed as evaluation metrics to measure the disparities between predicted and actual values. The visual representations of the results unmistakably demonstrated the superiority of the autoencoder LSTM model over both the CNN LSTM and LSTM models in all scenarios. The autoencoder LSTM consistently performed better than the other two models in terms of error rates and data resemblance, even though all three models displayed predicted behaviours. In terms of specific parameter predictions, the autoencoder LSTM model achieved an impressively low RMSE of 0.157 for daily power generation, while the CNN LSTM model had an RMSE of 0.188, and the LSTM model registered a higher RMSE of 0.312. A similar trend was observed for grid-connected power generation, where the autoencoder LSTM model achieved a noteworthy RMSE of 0.098, while the CNN LSTM model had an RMSE of 0.157. Finally, for the radiance parameter, the autoencoder LSTM model excelled with an RMSE of 0.15, surpassing the CNN LSTM model with an RMSE of 0.186 and the LSTM model with a higher RMSE of 0.236. This unequivocally underscores the autoencoder LSTM's capability to predict these three key parameters accurately. Moreover, it is important to note that the data visualisations were generated through a combination of 20% experimental data and 80% predictive data. The autoencoder LSTM consistently exhibited its ability to capture underlying patterns and trends, yielding more precise predictions for all three parameters.

By further enhancing these models through hybrid or ensemble techniques, we can establish a solid foundation for future advancements in renewable energy technologies and their seamless integration into the existing power infrastructure. These optimised models hold the potential to contribute significantly to the overall stability, reliability, and economic viability of renewable energy systems, paving the way for a greener and more sustainable future.

AUTHOR CONTRIBUTIONS

Ahsan Zafar: Conceptualization, methodology, software, data curation; writing – original draft. **Yanbo Che**: Methodology, formal analysis; supervision. **Muhammad Faheem**: Data curation, software, validation, review and editing. **Muhammad Abubakar**: Investigation; visualization. **Shujaat Ali**: Methodology; project administration. **Muhammad Shoaib Bhutta**: Conceptualization; resources.

ACKNOWLEDGEMENTS

The authors are highly grateful to their affiliated universities and institutes for providing research facilities and funding for this research work.

CONFLICT OF INTEREST STATEMENT

The authors declare no conflicts of interest.

DATA AVAILABILITY STATEMENT

The data will be available upon request to the corresponding author.

ORCID

Ahsan Zafar https://orcid.org/0000-0002-2981-9779
Muhammad Faheem https://orcid.org/0000-0003-4628-4486
Muhammad Shoaib Bhutta https://orcid.org/0000-0001-5176-3129

REFERENCES

1. Pal, R., et al.: A comprehensive review on IoT-based infrastructure for smart grid applications. IET Renew. Power Gener. 15(16), 3761–3776 (2021). https://doi.org/10.1049/rpg2.12272
2. Faheem, M., et al.: Smart grid communication and information technologies in the perspective of Industry 4.0: opportunities and challenges. Comput. Sci. Rev. 30, 1–30 (2018). https://doi.org/10.1016/j.cosrev.2018.08.001
3. Başaran, K., et al.: Systematic literature review of photovoltaic output power forecasting. IET Renew. Power Gener. 14(19), 3961–3973 (2020)
4. Sudharshan, K., et al.: Systematic review on impact of different irradiance forecasting techniques for solar energy prediction. Energies 15(17), 6267 (2022). https://doi.org/10.3390/en15176267
5. Chen, Y., et al.: Evaluation of machine learning models for smart grid parameters: performance analysis of ARIMA and bi-LSTM. Sustainability 15(11), 8555 (2023). https://doi.org/10.3390/su15118555
6. Kondaiah, V.Y., et al.: A review on short-term load forecasting models for micro-grid application. J. Eng. 2022(7), 665–689 (2022). https://doi.org/10.1049/tje2.12151
7. Abubakar, M., et al.: Performance analysis of energy production of large-scale solar plants based on artificial intelligence (machine learning) technique. Processes 10(9), 1843 (2022). https://doi.org/10.3390/pr10091843
8. Kim, E.G., Akhtar, M.S., Yang, O.-B.: Designing solar power generation output forecasting methods using time series algorithms. Elec. Power Syst. Res. 216, 109073 (2023). https://doi.org/10.1016/j.epsr.2022.109073
9. Faheem, M., Butt, R.A.: Big datasets of optical-wireless cyber-physical systems for optimizing manufacturing services in the internet of things-enabled industry 4.0. Data Brief 42, 108026 (2022). https://doi.org/10.1016/j.dib.2022.108026
10. Nazir, M.S., et al.: Optimized economic operation of energy storage integration using improved gravitational search algorithm and dual stage optimization. J. Energy Storage 50, 104591 (2022). https://doi.org/10.1016/j.est.2022.104591
11. Bhutta, M.S., et al.: Neuro-fuzzy based high-voltage DC model to optimize frequency stability of an offshore wind farm. Processes 11(7), 2049 (2023). https://doi.org/10.3390/pr11072049
12. Sarfraz, M., et al.: Recent analytical tools to mitigate carbon-based pollution: new insights by using wavelet coherence for a sustainable environment. Environ. Res. 212, 113074 (2022). https://doi.org/10.1016/j.envres.2022.113074
13. Ali, G., et al.: A hybrid convolutional neural network model for automatic diabetic retinopathy classification from fundus images. IEEE J. Transl. Eng. Health Med. 8(2), 1–10 (2023). https://doi.org/10.1109/jtehm.2023.3282104
14. Jamil, I., et al.: Predictive evaluation of solar energy variables for a large-scale solar power plant based on triple deep learning forecast models. Alex. Eng. J. 76, 51–73 (2023). https://doi.org/10.1016/j.aej.2023.06.023
15. Agga, A., et al.: CNN-LSTM: an efficient hybrid deep learning architecture for predicting short-term photovoltaic power production. Elec. Power Syst. Res. 208, 107908 (2022). https://doi.org/10.1016/j.epsr.2022.107908
16. Zheng, J., et al.: A hybrid framework for forecasting power generation of multiple renewable energy sources. Renew. Sustain. Energy Rev. 172, 113046 (2023). https://doi.org/10.1016/j.rser.2022.113046
17. Boussioux, L., et al.: Hurricane forecasting: a novel multimodal machine learning framework. Weather Forecast. 37(6), 817–831 (2022). https://doi.org/10.1175/waf-d-21-0091.1
18. Ren, Q., et al.: A novel deep learning prediction model for concrete dam displacements using interpretable mixed attention mechanism. Adv. Eng. Inf. 50, 101407 (2021). https://doi.org/10.1016/j.aei.2021.101407
19. Liang, J., Tang, W.: Ultra-short-term spatiotemporal forecasting of renewable resources: an attention temporal convolutional network-based approach. IEEE Trans. Smart Grid 13(5), 3798–3812 (2022). https://doi.org/10.1109/tsg.2022.3175451
20. Machalek, D., et al.: Dynamic energy system modeling using hybrid physics-based and machine learning encoder–decoder models. Energy AI 9, 100172 (2022). https://doi.org/10.1016/j.egyai.2022.100172
21. Mukhoty, B.P., Maurya, V., Shukla, S.K.: Sequence to sequence deep learning models for solar irradiation forecasting. In: 2019 IEEE Milan PowerTech., IEEE (2019)
22. Bahaghighat, M., et al.: Using machine learning and computer vision to estimate the angular velocity of wind turbines in smart grids remotely. Energy Rep. 7, 8561–8576 (2021). https://doi.org/10.1016/j.egyr.2021.07.077
23. Das, L., Garg, D., Srinivasan, B.: NeuralCompression: a machine learning approach to compress high frequency measurements in smart grid. Appl. Energy 257, 113966 (2020). https://doi.org/10.1016/j.apenergy.2019.113966
24. Zhang, Y., et al.: Data-driven day-ahead PV estimation using autoencoder-LSTM and persistence model. IEEE Trans. Ind. Appl. 56(6), 7185–7192 (2020). https://doi.org/10.1109/tia.2020.3025742
25. Neo, Y.Q., et al.: Forecasting of photovoltaic power using deep belief network. In: Tencon 2017-2017 IEEE Region 10 Conference, IEEE (2017)
26. Li, L.-L., et al.: Short-term output power forecasting of photovoltaic systems based on the deep belief net. Adv. Mech. Eng. 9(9), 1687814017715983 (2017). https://doi.org/10.1177/1687814017715983
27. Gensler, A., et al.: Deep learning for solar power forecasting—an approach using AutoEncoder and LSTM neural networks. In: 2016 IEEE International Conference on Systems, Man, and Cybernetics (SMC), IEEE (2016)
28. Abdel-Nasser, M., Mahmoud, K.: Accurate photovoltaic power forecasting models using deep LSTM-RNN. Neural Comput. Appl. 31, 2727–2740 (2019). https://doi.org/10.1007/s00521-017-3225-z
29. Zafar, A., et al.: Enhancing power generation forecasting in smart grids using hybrid Autoencoder long short-term memory machine learning model. IEEE Access 11, 118521–118537 (2023)
30. Said, Y., Alanazi, A.: AI-based solar energy forecasting for smart grid integration. Neural Comput. Appl. 35(11), 8625–8634 (2023). https://doi.org/10.1007/s00521-022-08160-x
31. Sabri, M., El Hassouni, M.: Photovoltaic power forecasting with a long short-term memory autoencoder networks. Soft Comput. 27, 1–21 (2023). https://doi.org/10.1007/s00500-023-08497-y

How to cite this article: Zafar, A., et al.: Machine learning autoencoder-based parameters prediction for solar power generation systems in smart grid. IET Smart Grid. 7(3), 328–350 (2024). https://doi.org/10.1049/stg2.12153